Short running title:

Adaptive actin networks ensure robust endocytosis

(50 characters, including spaces)

Full running title:

Adaptive actin organization counteracts elevated membrane tension to ensure robust endocytosis

(100 characters, including spaces)

Charlotte Kaplan[1], Sam J. Kenny[2], Shirley Chen[2], Johannes Schöneberg[1], Ewa Sitarska[3,§], Alba Diz-Muñoz[3], Ke Xu[2,4*] and David G. Drubin[1*]

[1]Department of Molecular and Cell Biology, University of California, Berkeley, CA 94720-3220

[2]Department of Chemistry, University of California, Berkeley, CA 94720-3220

[3]Cell Biology and Biophysics Unit, European Molecular Biology Laboratory Heidelberg, Meyerhofstrasse 1, 69117 Heidelberg

[4]Chan Zuckerberg Biohub, San Francisco, CA 94158.

[§] Collaboration for joint PhD degree between EMBL and Heidelberg University, Faculty of Biosciences

*Correspondence to DGD (drubin@berkeley.edu) or KX (xuk@berkeley.edu)

Manuscript for JCB article: 40,000 characters (not including spaces, methods, or references), with up to 10 figures and/or tables. Articles may have up to five supplemental items and references are unlimited.

Current number of characters 41,664 (no space)
Main Figures 8
2 Tables
Supp Figures 5
Supp movies 5

Highlights:

- Clathrin coat surface area and actin ultra-structure adapt to elevated membrane tension.
- The actin network is nucleated at the base of the clathrin-coated pit and grows upward.
- Actin ultra-structural organization is not tightly coupled to CME progression.
- Actin force generation is required earlier in CME progression under elevated membrane tension.

Summary (~40-word):

Kaplan et al. revealed that actin assembly compensates for changes in plasma membrane tension by an adaptive force generating mechanism to ensure robust endocytosis. Under elevated membrane tension the network grows deeper, even in early endocytic stages, from the base upward.

Abstract (160 words), 153 words

Clathrin-mediated endocytosis (CME) remains robust despite variations in plasma membrane tension. Actin assembly-mediated force generation becomes essential for CME under high membrane tension, but the underlying mechanisms are not understood. We investigated actin network ultrastructure at each stage of CME by super-resolution imaging. Actin and N-WASP spatial organization indicate that polymerization initiates at the base of clathrin-coated pits and that the actin network then grows away from the plasma membrane. Actin network organization is not tightly coupled to endocytic clathrin coat growth and deformation. Membrane tension-dependent changes in actin organization explain this uncoupling. Under elevated membrane tension, CME dynamics slow down and the actin network grows higher, resulting in greater coverage of the clathrin coat. This adaptive mechanism is especially crucial during the initial membrane curvature-generating stages of CME. Our findings reveal that adaptive force generation by the actin network ensures robust CME progression despite changes in plasma membrane tension.

Introduction

From yeast to humans, transient actin assembly is associated with the formation of clathrin-coated endocytic vesicles. In yeast cells, actin assembly is always required to generate forces to invaginate the plasma membrane against a high intrinsic turgor pressure for CME (Kaksonen, Sun, and Drubin 2003; Aghamohammadzadeh and Ayscough 2009; Idrissi et al. 2012; Kukulski et al. 2012). In mammalian cells, actin assembly augments CME and becomes increasingly critical as plasma membrane tension becomes increasingly elevated (Boulant et al. 2011; Kaur et al. 2014; Grassart et al. 2014). When actin assembly is perturbed in mammalian cells, CME typically slows in a cell-type-dependent manner (Fujimoto et al. 2000; Merrifield, Perrais, and Zenisek 2005; Grassart et al. 2014; Dambournet et al. 2018). A potential cause of this reported variation between cell types might be differences in plasma membrane tension (Pontes, Monzo, and Gauthier 2017). On an ultrastructural level, actin perturbation results in accumulation of "U-shaped" membrane invaginations, reflecting difficulty in progressing to the subsequent "omega-shaped" membrane stage (Fig. 1 A) (Fujimoto et al. 2000; Yarar, Waterman-Storer, and Schmid 2005; Boulant et al. 2011; Almeida-Souza et al. 2018). These findings suggest that actin assembly in general makes CME more efficient in mammalian cells, potentially compensating for changes in plasma membrane tension.

Despite the fact that actin assembly appears to be associated with CME in all eukaryotes and over a large range of membrane tensions, how actin assembly assists and whether it adapts to changes in membrane tension are not known. Key to addressing these questions is investigating the ultrastructure of actin networks at CME sites in vertebrate cells under different membrane tensions. Platinum replica electron microscopy of cultured cells has provided some insights into actin ultrastructure and force generation during mammalian CME (Collins et al. 2011). The

resulting electron micrographs led to the proposal that actin networks polymerize from a single mother filament and therefore assemble around clathrin coats asymmetrically, ultimately forming a collar-like arrangement around the vesicle neck (Fig. 1 A) (Collins et al. 2011). This actin organization suggested that a pushing force is generated orthogonal to the direction of membrane invagination, supporting neck constriction and fission. However, actin filaments do not only make interactions with the vesicle neck, but also with the bud surface, because the clathrin coat is embedded with actin-binding linker proteins like Hip1R and epsin, suggesting that actin filaments might also help to pull the forming vesicle into the cell (Engqvist-Goldstein et al. 2001; Messa et al. 2014; Sochacki et al. 2017; Clarke and Royle 2018).

Evidence suggests that such a pulling mechanism exists in budding yeast. Here, studies support a model in which actin filaments are nucleated in a ring at the surface of the plasma membrane surrounding the clathrin-coated pit (CCP), and in which the resulting filaments are coupled to the clathrin coat surface (Kaksonen, Sun, and Drubin 2003; Carroll et al. 2012; Skruzny et al. 2012, 2015; Picco et al. 2015; Mund et al. 2018). This assembly generates an inward force parallel to the plasma membrane invagination as the actin network grows away from the plasma membrane and pulls the coat with it against the high hydrostatic turgor pressure (Picco et al. 2015). The feasibility of this model is supported by mathematical models (Liu et al. 2009; Berro, Sirotkin, and Pollard 2010; Carlsson and Bayly 2014; Dmitrieff and Nédélec 2015; Wang and Carlsson 2017; Hassinger et al. 2017; Mund et al. 2018; Nickaeen et al. 2019; Akamatsu et al. 2020). Because the endocytic machinery is highly conserved from yeast to mammals, a similar mechanism for actin force generation seems likely to generate forces against membrane tension in mammalian CME. However, ultrastructural evidence for such an organization in mammalian CME, and for how this organization might respond to changing

membrane tension, are lacking. Importantly, several competing models for actin organization at CME sites in mammalian cells have been proposed, so it is now important to distinguish between these models (Engqvist-Goldstein et al. 2001; Messa et al. 2014; Sochacki et al. 2017; Clarke and Royle 2018; Boulant et al. 2011).

Here we used two-color, three-dimensional stochastic optical reconstruction microscopy (2c-3D STORM) to investigate actin organization at CME sites at different stages of internalization and established the relationship between actin organization and plasma membrane tension. We combined this method with live-cell imaging and experimental manipulations of membrane tension to investigate how elevated membrane tension affects actin network organization, and how actin assembly assists CME dynamics under a range of membrane tensions. Our data support an adaptive actin force-generating mechanism that ensures robust CME over a range of membrane tensions.

Results

Actin organization suggests that force generation can be either parallel to, or orthogonal to, or both, the axis of clathrin-coated pit formation at different sites in the same cell

Electron microscopy has been the method of choice to study actin ultra-structural organization at CME sites in mammalian cells (Collins et al. 2011; Akamatsu et al. 2020), but may not preserve all actin structures and is not amenable to achieving large sample sizes. Some electron microscopy (EM) procedures such as “unroofing” risk compromising structural integrity in order to obtain high resolution and unobstructed views. EM approaches can also lack the molecular specificity necessary to clearly identify specific proteins. Recent advances in super-resolution microscopy (SRM) provide new opportunities to examine cellular ultrastructures with low invasiveness and high molecular specificity (Sahl, Hell, and Jakobs 2017; Sigal, Zhou, and

Zhuang 2018). In particular, we have previously demonstrated the application of 3D-STORM to study actin and related membrane cytoskeletal systems in mammalian cells (Xu, Babcock, and Zhuang 2012; Xu, Zhong, and Zhuang 2013; Hauser et al. 2018) and CME in fission yeasts (Sun et al. 2019).

Here we reveal actin ultra-structural organization at clathrin-coated structures (CCSs) and clathrin-coated pits (CCPs) by 2c-3D STORM. Henceforth, we refer to CCSs as relatively flat clathrin structures and CCPs as curved, invaginating clathrin structures. Our 2c-3D STORM method preserves the sample by chemical fixation of intact cells, provides high molecular specificity due to immunofluorescence labeling, and allows large numbers of sites to be imaged.

We conducted our experiments on a skin-melanoma cell line (SK-MEL-2) wherein 87% of dynamin2-eGFP^{EN} (DNM2-eGFP^{EN}) spots appear together with actin at the ventral plasma membrane in live-cell fluorescence microscopy (Grassart et al. 2014). We previously used genome editing to generate a clone of this cell line expressing DNM2-eGFP^{EN} and clathrin light chain A-tagRFP-T (CLTA-TagRFP-T^{EN}) at endogenous levels (Doyon et al. 2011). We used this DNM2-eGFP^{EN}/ CLTA-TagRFP-T^{EN} cell line in our 2c-3D STORM experiments because it enabled us to complement our 2c-3D STORM data with live cell fluorescence microscopy using the same cell line.

We resolved CCSs as round and elliptical shapes on the ventral surface in these cells (Fig. 1 B). The majority of the CCSs appeared connected to filamentous actin visualized using Alexa Fluor 647-tagged phalloidin (phalloidin-AF647) (Fig. 1 C and D). When we zoomed into two representative clathrin coats, we could more clearly resolve the association with actin networks (Fig. 1 E shows blowups of boxed regions in Fig. 1 D).

Knowing how actin networks are organized spatially in all dimensions at CME sites provides insights into actin's force generation mechanism(s). We rendered the high-resolution CCSs in three-dimensions by cropping an area of 310 nm x 310 nm around each clathrin and actin structure's center of mass to generate an x-z STORM image projection. To our surprise we observed two strikingly different actin filament spatial organizations in the x-z projections of the first two clathrin coats we examined, even though they were near each other in the same cell (Fig. 1 D). In the first example, a thin layer of actin filaments resided at the base of the clathrin coat (Fig. 1 F, inset 1), reminiscent of structures observed in the EM by Collins *et al.*, 2011. In contrast, actin filaments covered the second CCP completely in the x-z projection (Fig. 1 F, inset 2). This organization resembles actin interacting with the whole clathrin coat as indicated by thin section electron micrographs and SRM in budding yeast (Mulholland et al. 1994; Idrissi et al. 2008; Kukulski et al. 2012; Buser and Drubin 2013; Mund et al. 2018). These data indicate that distinct actin structures can coexist in the same cell, consistent with models for force generation parallel to and orthogonal to the invagination axis.

CME site-associated actin networks grow from the CCP base to the tip of the coat and their organization is not coupled to CME progression

We next aimed to analyze how actin is organized at CME sites and asked how actin organization relates to progress through CME. We first determined when actin filaments are first detectable at CCSs and CCPs over the course of endocytosis by manually selecting 992 high-resolution clathrin coats after applying quality control criteria explained in the Materials and Methods (Fig. S1 A). In our cell line we could detect actin associated with 74% of the clathrin coats. We developed a procedure to determine the endocytic stage of each structure and then

used these staged structures to reconstruct a timeline of actin organization over the course of CME.

To classify the CME stages of the clathrin coats we used their x-z projections (side profiles), similar to what had been done previously by electron microscopy (Avinoam et al. 2015). Clathrin coats were classified as early, intermediate, or late invaginations as follows: using our STORM data, we measured clathrin coat width and height from x-z projections (Fig. 2 A, Fig. S1 B and C, see Materials and Methods). We then calculated the height to width ratios and defined a shape index (SI). We manually defined clathrin coats as early when they were shallowly curved and had a calculated SI index below 0.7 (Fig. 2 A and Fig. S1 D). Intermediate (U-shaped) clathrin coats had an SI index higher than 0.7 and lower than 0.9 (Fig. 2 A and Fig. S1 D). Late (omega-shaped) clathrin coats had a SI index higher than 0.9 (Fig. 2 A and Fig. S1 D). In representative x-z projections of clathrin coats we surprisingly could find a wide variety of actin organizations in each of the three categories of CME stages (Fig. 2 A). We concluded that irrespective of the endocytic stage at which the clathrin coats resided, we observed some that had a thin actin network at the base of the pit, others with an intermediate level of coverage of the clathrin, and others in which the actin completely covered the clathrin.

To extend our analysis to the entire data set, we quantified the overlap between clathrin and actin in all our x-z projections (see Materials and Methods). We then plotted the shape index versus the percentage of the clathrin coat covered by actin (Fig. 2 B). We could not detect a significant correlation between the endocytic stage, as reported by clathrin coat shape, and actin coverage of clathrin. This observation suggests that actin at individual CME sites in our cell type can polymerize at all endocytic stages: early, intermediate, and late.

While actin distribution did not appear to be coupled to the CME stage, it was variable in our data set. We found actin covering more than half the coat at 70% - 75% of clathrin sites in all three endocytic stages (Fig. 2 B). Accordingly, a significant fraction (25-30%) of clathrin sites at all stages had only partial actin coverage. We observed that whenever actin is only partially covering clathrin, the network is always located at the base of the clathrin coat (Fig. 2 A). This observation suggests that actin polymerization is nucleated at the base of the pit and that the network then grows upward to and over the top of the clathrin coat. To test the validity of this conclusion for the entire data set, we calculated the distance between the centroid of clathrin and actin in the x-z projection images for each individual site and plotted the distance against the clathrin coverage by actin as a percentage (Fig. 2 C, see Materials and Methods). As the actin average position minus the clathrin average position is negative when the coverage is low, but is near zero when the coverage is high, we concluded that actin polymerization is initiated at the base of clathrin coats.

To reinforce the conclusion that actin polymerization is first nucleated at the clathrin coat's base in early coats, we next investigated the spatial distribution of the actin nucleation factor N-WASP at clathrin coats by 2c-3D STORM. Consistent with our conclusions about where actin assembly occurs at CCPs, N-WASP localized to the base of both early clathrin coats and late clathrin coats (Fig. 2 D, Fig. S1 E). More unexpectedly, at some CME sites N-WASP covered the entire clathrin coat in early and late stages (Fig. 2 E, Fig. S1 E).

In summary, we conclude that actin polymerization is nucleated at the base of clathrin-coated pits and grows to the coat's tip. However, unexpectedly, actin nucleation is not coupled to the stage of CME progression. A possible explanation for the variety of actin organizations we

observed associated with clathrin coats is that the organization responds to changes in membrane tension to adapt the magnitude and orientation of forces produced.

Dynamics of clathrin-mediated endocytosis slow down under elevated membrane tension

We next aimed to use 2c-3D STORM to identify the stages of clathrin coat deformation to which actin force generation contributes under elevated membrane tension. Previous EM studies identified a requirement at the "U" to "omega" transition, but our light microscopy-based analysis of a large number of sites at many CME stages provided increased sensitivity for detecting effects throughout the process. To do so, we first needed to establish conditions under which CME dynamics are affected by elevated membrane tension in our genome-edited SK-MEL-2 cells.

We analyzed CME dynamics in the SK-MEL-2 cells by imaging DNM2-eGFP^{EN} and CLTA-TagRFP-T^{EN} in real time by total internal reflection microscopy (TIRF) and concomitantly, elevated membrane tension by hypotonic media treatment (Fig. 3 A). (Doyon et al. 2011). CLTA-TagRFP-T^{EN} and DNM2-eGFP^{EN} fluorescence lifetimes were determined by single-particle tracking. In cells imaged in isotonic media kymographs of CLTA-TagRFP-T^{EN} (magenta) and DNM2-eGFP^{EN} (green) fluorescence tracks reveal many relatively short clathrin tracks with a burst of DNM2-eGFP^{EN} signal at the end (Fig. 3 B, Supp. movie 1). For sites at which both CLTA-TagRFP-T^{EN} and DNM2-eGFP^{EN} were detected, the CLTA-TagRFP-T^{EN} and DNM2-eGFP^{EN} mean lifetimes were 47 ± 32.4 s (SD) and 38.8 ± 32.1 s (SD), respectively (Fig. 3 C and E). For CLTA-TagRFP-T^{EN} and DNM2-eGFP^{EN} tracks that were not associated with DNM2-eGFP^{EN} or CLTA-TagRFP-T^{EN}, respectively, mean lifetimes were 16.8 ± 11.8 s (SD) and 18.9 ± 12.3 s (SD), respectively, characteristic of structures not associated with CME (Fig. 3 D and F) (Hong, Cortesio, and Drubin 2015). Neither isotonic media nor exchange to slightly

dilute 225 mOsm media for 2 min prior to imaging noticeably affected DNM2-eGFP^{EN} and CLTA-TagRFP-T^{EN} lifetimes or CME initiation and completion rates for sites containing both proteins (Fig. S2 A - D). Only 1 - 2% of these CLTA-TagRFP-T^{EN} and DNM2-eGFP^{EN} fluorescence tracks persisted over the entire 4.8 min movie in isotonic and 225 mOsm media (Fig. S2 B and D).

An increase in CLTA-TagRFP-T^{EN} lifetime was observed in response to 2 min incubation in lower osmolarity 150 mOsm media, with a mean lifetime of 59.7 ± 52.7 s (SD) (compared to 49.1 ± 0.7 s for isotonic media exchange) (Fig. S2 E). In addition, mild effects on CME initiation rate: 14.7 ± 5.0 s (SD) (compared to 24.5 ± 6.3 s for isotonic media), completion rate: 10.7 ± 3.9 s (SD) (compared to 18.8 ± 6.0 s for isotonic media), and percentage of persistent tracks: 3.23 ± 1.3 % (SD) (compared to 0.77 ± 0.9 % (SD) for isotonic media) were observed but only after cells were cultured for 10 min in 150 mOsm media (Fig. S2 F).

We next tested the effect of exchange to 75 mOsm hypotonic media on CME dynamics. After 2 minutes in 75 mOsm hypotonic media a more dramatic effect was observed. Example kymographs of CLTA-TagRFP-T^{EN} (magenta) and DNM2-eGFP^{EN} (green) showed elongated fluorescence tracks that very often lasted over the entire duration of a 4.8 min movie (Fig. 3 B, Supp. movie 2). The mean lifetimes of CLTA-TagRFP-T^{EN} and DNM2-eGFP^{EN} tracks containing both proteins were 128.4 ± 111.9 s (SD) (Fig. 3 C) and 125.1 ± 111.5 s (SD), respectively (Fig. 3 E). We also observed a substantial decrease in CME initiation (2 min hypotonic: 10.28 ± 1.5 $\mu m^{-2}\,min^{-1}$ (SD) vs. isotonic: 22.18 ± 3.5 $\mu m^{-2}\,min^{-1}$ (SD)) and completion rates (2 min hypotonic: 5.32 ± 1.7 $\mu m^{-2}\,min^{-1}$ (SD) vs. isotonic: 17.75 ± 3.4 $\mu m^{-2}\,min^{-1}$ (SD)), together with a strong increase in the percentage of persistent tracks (2 min hypotonic: 19.17 ± 9.2 % (S.) vs. isotonic: 0.65 ± 0.3 % (SD)) over the 4.8 min duration of a movie (Fi. 3 G – I, Fig.

S2 G). After 10 min of culturing, the CLTA-TagRFP-T^{EN} and DNM2-eGFP^{EN} lifetimes began to recover, most likely reflecting cellular adaptation to the hypotonic treatment (Fig. 3 C, E and G-I, Supp. movie 3). We did not detect effects of hypotonic media treatment on lifetimes of tracks containing only CLTA-TagRFP-T^{EN} or only DNM2-eGFP^{EN} (Fig. 3 D and F). We conclude that CME dynamics are markedly reduced in SK-MEL-2 cells transferred to 150 mOsm media, with an even stronger effect observed with 75 mOsm media.

To determine how membrane tension is affected by changes in media osmolarity, we performed membrane tether pulling experiments by atomic force microscopy (AFM) on our cells cultured under isotonic conditions and at 75 mOsm. Under isotonic media conditions, we measured an average tether force of 33.0 ± 7.4 pN (SD). This value increased to 48.0 ± 17.1 pN (SD) in 75 mOsm media (Fig. 3 J). We exchanged the isotonic media with 75 mOsm hypotonic media on the sample stage and pulled tethers from cells beginning 2 min after media exchange and up to 16 min after media exchange. These experiments allow us to relate a quantitative change in membrane tension to effects on CME dynamics, actin and clathrin ultra-structural organization.

Actin force generation assists early clathrin coat deformation under elevated membrane tension

Next we wanted to investigate when in the process of CME branched actin filament assembly becomes important under elevated membrane tension. Branched actin networks are generated by the Arp2/3 complex and activated by N-WASP (Pollard 2007). We inhibited Arp2/3-mediated actin polymerization using the small molecule CK666 (Hetrick et al. 2013). Since Arp2/3 inhibition can affect membrane tension (Diz-Muñoz et al. 2016), we first carefully established the experimental conditions so the effects of high membrane tension or CK666

would not mask one another. Once conditions were optimized, we performed STORM image analysis to learn more about the CME stages at which branched actin network assembly is required.

We first titrated CK666 and monitored the effect on CME dynamics in a 4.8-minute movie starting after 2 min of CK666 treatment. We aimed to identify a minimal CK666 concentration that would show a rapid effect on CME dynamics. 100μM CK666 extended lifetimes of CLTA-TagRFP-T^{EN} associated with DNM2-eGFP^{EN} to 78.9 ± 66.2 s (SD) after 2 mins of treatment compared to 56.2 ± 39.9 s for the DMSO control (Fig. S3 A)). 100μM CK666 did not affect CME completion frequency and therefore we also detected no increase in the percentage of persistent CLTA-TagRFP-T^{EN} tracks (Fig. S3 B and C), though we observed a small decrease in the CME initiation rate (Fig. S3 D).

Kymographs showing the DNM2-eGFP^{EN} and CLTA-TagRFP-T^{EN} fluorescence signals revealed elongated tracks upon 100μM CK666 treatment, with further elongation observed upon simultaneous osmotic elevation of membrane tension (Fig. 4 A). As quantitatively analyzed in Fig. 4B-E, compared to controls (Fig. 4 B and D) the combination of 100μM CK666 and elevated membrane tension markedly lengthened the lifetimes of clathrin 96.3 ± 85.5 s (SD) (compared to DMSO control 59.0 ± 51.9 s (SD)) and dynamin2 83.5 ± 85.3 s (SD) (compared to DMSO control 46.9 ± 48.8 s (SD)) associated with each other at CME sites (Fig. 4 C and E). Consistent with the results of Boulant et al. (2011), who examined the effects of actin inhibitors on CME when membrane tension is elevated, our results reveal that Arp2/3 complex-mediated actin assembly is required for normal CME dynamics under elevated membrane tension.

We next sought to determine the precise CME stages during which Arp2/3-branched actin network force contributes to normal progression when membrane tension is elevated. We

used STORM to look for increased representation of CME stages upon drug and osmolarity treatment. Cells were treated under the optimized CK666 and osmolarity conditions described above, chemically fixed, and then immunolabeled for clathrin. CME sites in the STORM images were staged using criteria described in Fig. 2 above, and their height and width in x-z projections were quantified (Fig. 4 F). As in the above 2d-3D STORM experiments, the full progression from a flat clathrin coat to a rounded vesicle could be clearly resolved in the x-z projections (Fig. 4 F, lower image panel). Here, we used clathrin coat height as a proxy to precisely quantify when clathrin coat progression is affected. Control cells treated with DMSO showed an average clathrin coat height of 98 ± 21 nm (SD) (Fig. 4 G, Fig. S3 E). The average height increased to 106 ± 27 nm (SD) when cells were treated with 100μM CK666, consistent with previous studies reporting a high accumulation of U-shaped clathrin coats in electron micrographs of epithelial cells treated with Latrunculin A and Jasplakinolide (Boulant et al. 2011).

Interestingly, when Arp2/3-mediated actin polymerization was inhibited in cells with elevated membrane tension, the average clathrin coat height decreased to 96 nm ± 24 nm (SD) (Fig. 4 G, Fig. S3 E). This height decrease was also reflected in the accumulation of smaller shape indices compared to 100μM CK666 only treatment, together with a very mild effect on clathrin coat width (Fig. S3 E – G). This result indicates that the transition from a shallow invaginated coat to a U-shaped coat is slowed when Arp2/3-mediated actin filament assembly is inhibited in cells with elevated membrane tension.

The above data support the conclusion that Arp2/3-mediated actin force generation facilitates the U-shaped to omega-shaped clathrin coat transition under isotonic conditions, but becomes critical for the early transition from a shallow invaginated to U-shaped coat when membrane tension increases.

352 ***Contribution of clathrin coat surface area to membrane remodeling***

353 Clathrin coat assembly can provide energy to bend the plasma membrane (Kaksonen and
354 Roux 2018; Sochacki and Taraska 2019). Since we are able to extract clathrin height and width
355 from our STORM data, we asked whether we detected an effect on clathrin coat surface area
356 when membrane tension is elevated. Mathematical simulations suggest that when the membrane
357 tension is low, increasing the clathrin coat area can provide sufficient energy for membrane
358 vesicle formation (Hassinger et al. 2017). In addition, clathrin can polymerize into a fully formed
359 pit on giant unilamellar vesicles under hypertonic media conditions (Saleem et al. 2015). Indeed,
360 we find that 26% of our super-resolved clathrin coats in all stages of CME lacked detectable
361 actin (Fig. 5 A and B, Fig. S 4 A and B). Of the clathrin coats lacking detectable actin, 5% show
362 an associated diffraction-limited DNM2-eGFP^{EN} signal (Fig. 5 B and Fig. S4 B). The DNM2-
363 eGFP^{EN} fluorescence serves as a read-out for membrane vesicle neck formation (Avinoam et al.
364 2015; Sochacki et al. 2017). We assume that fully formed clathrin coats without actin or DNM2-
365 eGFP^{EN} were either going to become associated with DNM2-eGFP^{EN} or were already associated
366 with DNM2-eGFP^{EN} and recently underwent vesicle scission. Therefore, this is a population
367 represented among the CLTA-TagRFP-T^{EN} and DNM2-eGFP^{EN} associated tracks that we
368 observe in living cells, and we included them when performing our analysis of clathrin coat
369 surface area. By classifying clathrin coats as being or not being associated with DNM2-eGFP^{EN},
370 and using the shape index information, we were able to organize the coats lacking actin into
371 early, intermediate, membrane fission or later (after membrane fission) (Fig. 5 C).
372 For the clathrin coats showing detectable actin, 50% contained a DNM2-eGFP^{EN} fluorescence
373 signal (Fig. 5 D and E, Fig. S 4 C and D). We used the same classification to place each structure
374 analyzed into a timeline as we did for the coats without actin (Fig. 5 F). As described below, this

375 classification enabled the detection of differences in clathrin coat surface area, not only
376 depending on membrane tension but also on actin.

377 Upon sorting the individual CCSs and CCPs into positions along the above established
378 timeline, we first found that under isotonic media conditions the coat surface area on average
379 increased in the transition from early (Without actin: 62055 ± 16951 nm^2 (SD), and with actin
380 54811 ± 17328 nm^2 (SD)) to intermediate endocytic stage (Without actin: 71048 ± 18854 nm^2
381 (SD), and with actin 61145 ± 17360 nm^2 (SD)) (Fig. 6 A and C and Table 1). This increase in
382 surface area was independent of actin. In subsequent endocytic stages, we did not detect any
383 changes in average coat surface area. We conclude that clathrin polymerization to enlarge the
384 coat surface area is likely to contribute energy to membrane bending in the transition from early
385 to intermediate endocytic stages, but then the coat surface area remains constant until final CCV
386 formation.

387 Under 75 mOsm hypotonic media conditions, the difference in coat surface area between
388 the early and intermediate stages vanished. However, we detected on average a substantially
389 larger surface coat area between the early-intermediate (Without actin: 69606 ± 17353 nm^2 (SD),
390 and with actin 68347 ± 21643 nm^2 (SD)) and the membrane fission stage (Without actin: 80071
391 ± 26077 nm^2 (SD), and with actin 73414 ± 25636 nm^2 (SD)) (Fig. 6 B and D and Table 1). After
392 fission, the coat surface area decreased again (Without actin: 67607 ± 22633 nm^2 (SD), and with
393 actin 59022 ± 22969 nm^2 (SD)) (Table 1). We speculate that in the early stages the clathrin coat
394 surface area must increase to a certain threshold to drive membrane bending under higher
395 membrane tension. Subsequent coat growth contributes energy for the U-shape to omega shape
396 transition of the clathrin coats. We observed similar surface area changes under hypotonic media
397 conditions irrespective of whether actin was present or lacking. However, the magnitude of the

coat surface area change was larger when actin was present (Table 1). We speculate that these clathrin sites might have experienced locally higher membrane tension, reflected in the induction of actin assembly.

Interestingly, we also observed that on average, the clathrin coat surface area was smaller when actin was present compared to when actin was absent (Fig. 6A-D and Table 1). Under isotonic conditions this difference was observed for each of the stages of endocytosis. Whereas under hypotonic media conditions the coat surface area was smaller when actin was present, this difference was not statistically significant. We conclude that when actin is absent, the coat surface areas grow larger, possibly to contribute the energy required for membrane bending. When actin was present we speculate that it either contributes enough force to bend the membrane so further growth of the clathrin coat surface area is not necessary. Therefore, the coat surface area is on average smaller for each stage of endocytosis. On the other hand, when actin is present at the cortex this might restrict the clathrin coats from expanding their surface area.

Thirdly, we compared the average clathrin coat surface area between the isotonic media condition (low membrane tension) and the 75 mOsm hypotonic media condition (high membrane tension) over the course of endocytosis (Fig. S4 E). In the absence of actin, the average coat surface area under higher membrane tension was larger even in the early stage (Hypotonic: 69456 ± 20014 nm^2 (SD), isotonic: 62055 ± 16951 nm^2 (SD)) (Fig. 6 A and B, Fig. S4 E, Table 1). Over the remaining stages of endocytosis, the coat surface area still showed the trend to be on average either at the same size or of slightly larger size under higher membrane tension.

We detected a much larger difference between the coat surface area at low and high membrane tension when actin was present. From the early stage to the membrane fission stage, the average coat surface area was considerably larger when membrane tension was higher (Fig.

S4 E). These results are consistent with the possibility that clathrin polymerizes to cover a larger surface area under higher membrane tension to contribute energy to membrane remodeling.

Taken together, clathrin coat surface area differs depending on whether actin is present or absent, and on membrane tension. Our results suggest that the clathrin coat surface area might contribute to an adaptive force generating mechanism that responds to changes in membrane tension.

Actin organization adapts to elevated membrane tension by increasing coverage of clathrin coats

We found evidence that actin force generation contributes to the progression of early stages of CME under elevated tension. Since 75mOsm hypotonic media caused a pronounced slowdown of CME dynamics after only 2 min in our live cell experiments and strongly increased membrane tension of our SK-MEL-2 cells, we applied this same treatment to the cells and then chemically fixed them for 2c-3D STORM. When we super-resolved clathrin and actin by 2c-3D STORM in cells treated with 75 mOsm hypotonic media, the actin cytoskeleton remained intact and associated with CCSs (Fig. S5 A - D).

We observed that the average actin height dramatically increased for all endocytic stages after membrane tension was elevated by switching to 75 mOsm hypotonic media (Fig. 7 A and B, Table 2). In early clathrin coats, the average actin height increased from 123 nm ± 29 nm (SD) under isotonic media conditions to 158 nm ± 48 nm (SD). This growth of the actin network correlated well with an increase of average clathrin coverage by actin at early coats from 66% to 76% under 75 mOsm hypotonic media (Fig. 7 C, Table 2). Likewise, actin height and coat coverage of intermediate coats also increased significantly (Fig. 7 B, C and Table 2).

443 The average actin network height for clathrin coats at membrane fission reaches 161 nm
444 ± 39 nm (SD) under hypotonic media treatment, which differs dramatically from the height 135
445 nm ± 30 nm (SD) under isotonic conditions (Fig. 7B, Table 2). Actin covering clathrin coats at
446 membrane fission on average showed a moderate increase from 64% to 69% under hypotonic
447 conditions (Fig. 7C). The difference in average clathrin coverage of actin was even greater for
448 late coats (65% to 73%). These observations of higher average actin height and clathrin coverage
449 at late clathrin coats suggest that the force contribution of actin in late CME around the time of
450 vesicle scission is increased when membrane tension is elevated.

451 In response to hypotonic media treatment, actin was observed to grow over the clathrin
452 coats of all stages and, consistently, the actin network height increased as well (Fig. 7D and E,
453 Fig. S5 E and F). When we then plotted actin height against clathrin coverage, we found that on
454 average, actin height is also greater even when coverage of clathrin is in the lower percentage
455 range (Fig. 7 F and G). Our observations suggest that the actin network grows higher at clathrin
456 sites under elevated membrane tension by growing over the clathrin-coated pit and also towards
457 the plasma membrane.

458 Based on electron micrographs, it has been proposed that actin filaments envelope
459 clathrin coats asymmetrically in mammalian cells (Collins et al. 2011). We wanted to evaluate
460 whether higher symmetry around the clathrin coat might also contribute to higher force
461 generation. Therefore, we determined the position of the maximum actin signal for normalized x-
462 histogram intensity from x-z and y-z STORM image projections and calculated the distance of
463 the signal's maximum from the clathrin coat's center (Fig. 7 H, Fig. S5 G, see Materials and
464 Methods). Early stage coats under isotonic media conditions showed a wide distribution of actin
465 signal deviation from the center with a mean of 99.2 ± 51 nm (SD). Actin symmetry increased

for intermediate clathrin coats and coats undergoing membrane fission (intermediate clathrin coat mean 84.1 nm ± 49 nm (SD); membrane fission clathrin coat mean 73.6 nm ± 49 nm (SD)). Interestingly, late clathrin coats after fission showed a more asymmetric actin organization (Mean 84.7 ± 52 nm (SD)), again. These data indicate that actin polymerization at the clathrin coat's base starts off asymmetrical and reaches the highest symmetry at membrane fission. That the symmetric actin organization was decreased in the late clathrin coats after membrane fission might indicate a rearrangement of actin organization after vesicle scission, perhaps to propel the released vesicle into and through the cytoplasm.

We observed that under hypotonic media treatment, compared to isotonic conditions, actin networks grew more symmetrically even around the early coats (72.4 nm ± 44 nm (SD). This parameter did not change appreciably during CME progression (Fig. 7 I and Fig. S5 H).

Overall, these observations lead us to conclude that actin grows higher in the z-dimension at clathrin coats under elevated plasma membrane tension, the actin networks are more symmetric and they achieve higher clathrin coat coverage. Such an adaptive mechanism for actin organization presumably generates the required forces to ensure efficient progression of mammalian CME under varying membrane tensions.

Discussion

By combining two-color, three-dimensional STORM imaging, quantitative live-cell TIRF microscopy, and membrane tension measurements by AFM membrane tether pulling experiments, we showed that actin organization and clathrin coat area adapt to membrane tension changes at individual CME sites. This mechanism likely generates forces necessary for robust endocytic progression over a range of membrane tension regimes. While STORM that we

applied to resolve individual CCSs cannot attain the resolution of EM, our approach had several advantages that allowed us to gain these new mechanistic insights; (1) it allowed us to sample much larger numbers of CME sites than is possible by EM, (2) we imaged the CME sites in intact cells that had not been subjected to unroofing or extraction protocols, and (3) we were able to use antibodies and fluorescent phalloidin to unambiguously identify specific proteins at CME sites.

Actin assembly and organization adapt to elevated membrane tension

We and others showed that elevating membrane tension can have a dramatic impact on CME dynamic progression in mammalian cells (Raucher and Sheetz 1999; Boulant et al. 2011; J. P. Ferguson et al. 2016, 2017; Willy et al. 2017; Bucher et al. 2018). Our results provide mechanistic insights into how the CME machinery adapts to elevated membrane tension to maintain robust CME progression. We showed that actin began to polymerize and that the amount of assembly and network organization adapted to membrane tension for three membrane tension regimes as defined by Hassinger et al. (2017) and now refined by our data obtained from measuring membrane tension of SK-MEL-2 cells by AFM membrane tether pulling (Fig. 8). It is important to note that these tension regimes do not necessarily apply to distinct cells. Since we detect differences in actin organization at individual CME sites within a single cell by 2c-3D STORM, these different membrane tension regimes might reflect local differences in tension within a single cell.

Low membrane tension regime

Clathrin coat assembly provides sufficient energy to bend the underlying plasma membrane into a full spherical shape when membrane tension is low (Fig. 8) (Saleem et al. 2015). We indeed found in our STORM data that 26% of clathrin coats are without actin in early,

intermediate and late CME stages. We further found that the clathrin coat area measured by STORM is on average larger when there is no associated actin. This observation is consistent with mathematical modeling, which indicates that an increased coat area can provide sufficient energy to bend the plasma membrane when membrane tension is low (0.002 pN/nm, (Hassinger et al. 2017)). Since 26% of the super-resolved clathrin coat structures were not associated with actin, we defined our low membrane tension regime as being below the tether force value of 27.5 pN This tether force value marks the upper border of 25% of the tether force values that are equal to and smaller than 27.5 pN in the plot in Figure 3 J for cells cultured in isotonic media. Assuming a 100 pN*nm bending rigidity of the plasma membrane, the calculated membrane tension for 27.5 pN is 0.096 pN/nm (Diz-Muñoz, Fletcher, and Weiner 2013). A small population of the super-resolved clathrin coats lacking associated actin are associated with dynamin2, which indicated that they undergo membrane neck formation and, presumably, scission. Interestingly, the CME sites that did not have detectable actin generally showed a very low actin cortex density in the x-y STORM image projections (Fig. S4 A and B). The lack of an actin cortex in those regions might reflect a lower membrane tension and therefore lack of a need for actin assembly in this membrane tension regime.

Intermediate tension regime

When membrane tension was elevated to an intermediate level, CME lifetimes slowed. 74% of super-resolved clathrin coats were associated with actin. When we observed clathrin coats in the late endocytic stage, 25% showed an actin coverage below 50% (Fig. 2 B). Therefore, we define the intermediate tension regime as being between the low membrane tension regime 0.096 pN/nm defined above and the measured average membrane tether force of 33 pN under isotonic media condition, resulting in a calculated membrane tension of 0.14 pN/nm

(when using a bending rigidity of 100 pN*nm). Clathrin coat assembly and membrane curvature inducing proteins still appear to provide sufficient energy to drive the shallow to U-shaped clathrin coat transition (Fig. 8, intermediate membrane tension). In addition, when we inhibited Arp2/3-mediated actin polymerization using CK666, clathrin coat progression stalled at the U-shaped stage, consistent with the effects of actin assembly inhibition in other cell types (Yarar, Waterman-Storer, and Schmid 2005; Boulant et al. 2011; Almeida-Souza et al. 2018). Thus, at intermediate membrane tension it appears that actin force generation is primarily required for the U-shaped to omega-shaped clathrin coat transition. The actin network organization at the base of the pit is well positioned to drive plasma membrane neck constriction and scission by generating forces orthogonal to the direction of membrane invagination.

High membrane tension regime

Our STORM observations indicate that as membrane tension is elevated further, actin force generation increasingly becomes required to drive coat deformation and membrane invagination during the early stages of CME (Fig. 8). We found that for 70% of early endocytic sites under isotonic conditions, actin covered over 50% of the coat surface area (Fig. 2 B). This higher membrane tension regime presumably starts above our measured mean calculated membrane tension of 0.14 pN/nm. When we inhibited Arp2/3-mediated actin polymerization using CK666 under high membrane tension, we found that coat deformation slows in the shallow coat regime. Actin assembly from the base of the CCP continues until the network covers the clathrin coat completely, allowing it to interact with proteins linking the actin network to the clathrin coat (Engqvist-Goldstein et al. 2001; Sochacki et al. 2017; Messa et al. 2014). Actin-binding linker proteins such as Hip1R and epsin1 cover the clathrin coat completely where they

557 are positioned to provide high membrane internalization efficiency by harnessing actin assembly
558 forces perpendicular to the plasma membrane (Akamatsu et al. 2020).

559 When the actin network fully covers the clathrin coat it resembled the radial organization
560 described by mathematical modeling for mammalian CME and the actin network organization
561 described for budding yeast (S. M. Ferguson et al. 2009; Hassinger et al. 2017; Mund et al. 2018;
562 Akamatsu et al. 2020). In yeast this actin organization drives endocytic membrane invagination
563 against the high resistance resulting from turgor pressure. Mathematical modeling showed that
564 this organization provides high forces perpendicular to the plasma membrane (Hassinger et al.
565 2017). Actin-generated forces parallel and orthogonal to the membrane invagination at high
566 tension may coexist to drive membrane invagination first and then scission.

567 Under high hypotonic media conditions such as 75 mOsm, we measured a mean tether
568 force of 48 pN that results in a mean membrane tension of 0.29 pN/nm (using 100 pN*nm as
569 bending rigidity for the calculation). CME dynamics dramatically slowed down when cells were
570 in this high membrane tension regime resulting in only ~40% of endocytic lifetimes that were
571 shorter than 50 sec and ~19% were longer than the 4.8 min movies we captured (Fig. 3 C). We
572 suggest here that we observed the limits of this adaptive mechanism that could have potentially
573 severe impact on dysregulation of the endocytic process.

574 **Clathrin coat surface area also responds to membrane tension and might contribute**
575 **energetically to membrane deformation**

576 Clathrin coat assembly and growth in area contribute energetically to membrane bending
577 (Saleem et al. 2015; Hassinger et al. 2017). In agreement with theoretical modeling and in vitro
578 findings, our STORM data revealed that the average clathrin coat surface area increased with

579 increasing membrane tension. Hence the clathrin coat itself might also be part of the adaptive
580 mechanism that responds to changes in membrane tension.

581 Mathematical modeling shows that under low membrane tension (0.002 pN/nm) an
582 average coat area increase of 9000 nm^2 can drive step-wise membrane remodeling from flat to
583 U-shaped and U-shaped to membrane neck closure (Hassinger et al. 2017). However, under the
584 model's defined high membrane tension (0.2 pN/nm), a surface of 28000 nm^2 alone does not
585 provide sufficient energy to achieve a flat to curved membrane transition. We and others
586 observed that the average clathrin coat surface area increased under high membrane tension
587 caused by hypotonic media conditions and thus appears to contribute energy for membrane
588 bending (Willy et al. 2019). In addition, we and others also found coat surface areas were larger
589 than the 28 000 nm^2 used in mathematical modeling studies, even under isotonic media
590 conditions when our SK-MEL-2 cells are at their equilibrated membrane tension of 0.14 pN/nm
591 (Avinoam et al. 2015; Bucher et al. 2018). Therefore, we speculate that when larger clathrin coat
592 surface areas are observed, the cells being observed might be experiencing either global or local
593 regions of higher membrane tension (> 0.14 pN/nm).

594 Interestingly, we measured the same average growth in clathrin coat surface area in cells
595 as was predicted by mathematical modeling to be necessary to drive the development of
596 membrane curvature. Under isotonic media conditions we detected an average growth of coat
597 surface area of 8993 nm^2 without actin and 6334 nm^2 when actin was present from the early into
598 the intermediate stage (Hassinger et al. 2017; Bucher et al. 2018). This observation can be
599 explained if actin compensates for membrane bending energy loss when there is less coat
600 growth. As has previously been reported for the same SK-MEL-2 cells that we use in our study,

601 the surface coat area stays constant throughout the remaining endocytic stages under isotonic
602 media conditions (Avinoam et al. 2015).

603 When we elevated membrane tension to 0.29 pN/nm by hypotonic media treatment, we
604 observed on average a larger surface area by approx. 7600 nm^2 in the early endocytic stage. At
605 the beginning of membrane neck formation this difference in surface area under elevated
606 membrane tension increased on average to approx. 10700 nm^2. These coat surface area
607 differences under elevated membrane tension appeared independent of actin. This observation
608 suggests that the increase in coat area contributes membrane bending energy to compensate for
609 increases in plasma membrane tension, as supported by the results reported here and elsewhere
610 (Willy et al. 2019).

611 **N-WASP spatial organization suggests an actin force generation control mechanism**

612 N-WASP spatial organization at CCSs and CCPs provides valuable mechanistic insight
613 into how actin network assembly contributes to force generation during CME. We found that N-
614 WASP localized at the base of early and late clathrin-coated pits, where it likely interacts with
615 SH3 domain-containing proteins present at the endocytic membrane neck (Schöneberg et al.
616 2017; Sochacki et al. 2017; Almeida-Souza et al. 2018). This organization is similar to that of the
617 homologous nucleation promoting factor Las17 in budding yeast (Mund et al. 2018). Filaments
618 nucleated at the base of CCPs would be able to interact with coat proteins such as Hip1R and
619 Epsin1/2/3 to generate forces to invaginate the plasma membrane (Hassinger et al. 2017; Mund
620 et al. 2018; Akamatsu et al. 2020). N-WASP at the base of CCPs is expected to activate the
621 Arp2/3 complex to nucleate actin networks to generate forces both orthogonal and parallel to the
622 plasma membrane to drive invagination and membrane neck closure, respectively.

623 Intriguingly, we also sometimes observed a strikingly different N-WASP spatial
624 organization in which it was distributed over the full clathrin coat. The type II nucleation factors
625 Abp1 and cortactin bind to actin filaments and to the Arp2/3 complex and could serve as binding
626 partners for N-WASP when actin surrounds the clathrin-coated pit (Le Clainche et al. 2007;
627 Pinyol et al. 2007; Helgeson and Nolen 2013; Guo et al. 2018). Such an organization might
628 reflect a distinct mechanism of actin filament assembly from the coat that is potentially important
629 to generate higher forces when actin already surrounds the clathrin-coated pit.

630 The results presented here provide a new understanding of how actin functions in
631 mammalian clathrin-mediated endocytosis by adapting its ultrastructural organization to changes
632 in plasma membrane tension, thereby ensuring the progression of a flat clathrin-coat to a round
633 clathrin-coated vesicle. Clathrin-coat surface area also responds to these changes in plasma
634 membrane tension. Future studies will be required to determine how clathrin machinery
635 components contribute to this adaptive mechanism.

636

637 **Materials and Methods:**

638

639 **Cell culture**: SK-MEL-2 cells from clone Ti13 (hCLTA^{EN-1} /hDNM2^{EN-1}) were cultured in
640 DMEM/F12 with GlutaMax™ supplement (10565-018, Thermo Fisher Scientific) media
641 containing 10% fetal bovine serum (FBS) and 1,000 U/mL penicillin-streptomycin mix
642 (15140122, Thermo Fisher Scientific) and kept in a 37°C humidified incubator with 5% CO2
643 (cell source information (Doyon et al. 2011)). After each cell vial was thawed, cells were
644 checked after 2 passages for mycoplasma contamination. Cell line authentication was performed
645 by short tandem repeat validation.

646

647 **Antibodies and reagents**: The primary antibodies used were mouse anti-clathrin light chain (AB
648 CON.1, MA5-11860, Thermo Fisher Scientific), mouse anti-clathrin heavy chain (AB X-22,

MA1-065, Thermo Fisher Scientific) and rabbit anti-N-WASP (ab126626, Abcam). The secondary antibodies used were Alexa Fluorophore 647 chicken anti-rabbit (A21443, Thermo Fischer Scientific), goat anti-mouse (115-005-205, Jackson ImmunoResearch) conjugated to CF680-NHS ester (Biotium 92139). Reagents and small molecule inhibitors used were DMSO (D2650, Sigma Aldrich), CK666 (SML0006, batch # 0000012761, Sigma Aldrich) and Phalloidin -AF647 (A22287, Fisher Scientific).

Preparation of CF680-labeled secondary goat anti-mouse antibody: CF680 NHS ester was dissolved at a concentration of 3 mM in anhydrous DMSO. 1 µL of dye solution, 80 µL of a 1.25 mg/mL suspension of unlabeled goat anti-mouse IgG1 secondary antibody (115-005-205, Jackson ImmunoResearch Laboratories, Inc.), and 10 µL of 1M sodium bicarbonate solution were mixed and allowed to react for 15 min at room temperature. The reaction mixture was added to an equilibrated NAP-5 column (Sigma GE17-0853-01) and flushed with PBS. The dye conjugated antibody was collected from the first colored eluent fraction and a concentration of 0.12mg/mL was determined with a NanoDrop spectrophotometer.

Sample preparation for two-color clathrin and actin imaging; 18 mm round coverslips were cleaned 20 min in 70% ethanol (Electron Microscopy Science, Cat # 72222-01). Cells were detached with 500uL 0.05% trypsin (25300-054, Gibco), washed once in DMEM/F12 and collected by centrifugation. Cells were counted using a hemocytometer and 20,000 cells/mL were seeded onto 18 mm round coverslips in 12-well plates. Cells were incubated for 16 – 24 hours in culture media prior to preparation for imaging.

Cells were fixed first for 1-2 min in 0.3% (v/v) glutaraldehyde (GA) solution containing 0.25% (v/v) Triton in cytoskeleton buffer (CB: 10mM MES, 150mM NaCl, 5mM EGTA, 5mM Glucose, 5mM $MgCl_2$, 0.005% NaN_3, pH6.1) and then immediately fixed for 10 min in 2% (v/v) GA solution in CB. Both solutions were prepared fresh from a 70% GA stock (Electron Microscopy Science, cat #16365) (protocol follows reference (Xu, Babcock, & Zhuang, 2012)). After fixation, samples were washed once in CB and then incubated for 7 min in freshly prepared CB containing 0.1% (w/v) $NaBH_4$. Subsequently, samples were washed 3 times for 10 min in CB with gentle agitation on a shaker. Samples were then blocked for 30 min in 5% (w/v) BSA in CB (Sigma Aldrich, A3733). For dense clathrin labeling, light (diluted 1:200) and heavy chain

(diluted 1:200) antibodies were used together in a 1% (w/v) BSA CB solution. Primary antibody immunostaining was performed overnight at 4°C. On the next day, samples were washed twice in 1% (w/v) BSA CB for 5 min. The mouse secondary antibody-CF680 was used at a final concentration of 0.40 µg/mL – 0.60 µg/mL in a 1% BSA - 1x CB solution. Samples were stained for 30 min at room temperature in the dark and washed twice for 5 min in 1% (w/v) BSA CB solution, and then for 10 min in CB solution. Samples were then placed into a solution of CB containing 0.5µM Phalloidin-AF647 and kept at room temperature in the dark for a minimum of 2 hours. Samples were washed once with PBS before STORM imaging.

Sample preparation for single-color clathrin and dual-color N-WASP imaging: Cells were prepared as for the two-color sample preparation on coverslips, and then fixed for 20 minutes in 3% (v/v) paraformaldehyde (PFA, 15710 Electron Microscopy Sciences) in CB (protocol follows (Li et al. 2018)). Samples were washed quickly in CB and subsequently were incubated for 7 min in freshly prepared 0.1% (w/v) $NaBH_4$ in CB solution. Subsequently, samples were washed 3 times for 10 min in CB with gentle agitation on a shaker and permeabilized afterwards in a 0.1% Triton-PBS solution for 1-2 min. For single antibody clathrin staining, subsequent washing, blocking and antibody incubation steps were similar to the two-color clathrin and actin sample preparation protocol.

Dual-color immunolabeling was performed with primary antibody against N-WASP (diluted 1:200), clathrin heavy and clathrin light chain (diluted 1:600 -1:1000) in 1% (w/v) BSA in PBS over night at 4°C. Samples were washed the next day twice for 5 min in 1% (w/v) BSA in PBS. Secondary antibody staining was first performed with Alexa Fluorophore 647 anti-rabbit antibody (diluted 1:200) in 1% BSA (w/v) in PBS for 30 min at room temperature and kept in the dark. After two 10 min long washes in PBS containing 1% (w/v) BSA, secondary antibody staining was performed with CF680 anti-mouse antibody (diluted 1:600). The samples were given three final washes in PBS for 10 min each.

SRM imaging: Dye-labeled cell samples were mounted on glass slides in a standard STORM imaging buffer consisting of 5% (w/v) glucose, 100 mM cysteamine, 0.8 mg/mL glucose oxidase, and 40 µg/mL catalase in 1M Tris- HCL (pH 7.5) (Huang et al, 2008; Rust et al, 2006). Coverslips were sealed using Cytoseal 60. STORM imaging was performed on a

homebuilt setup (Wojcik et al. 2015) based on a modified Nikon Eclipse Ti-U inverted fluorescence microscope using a Nikon CFI Plan Apo λ 100x oil immersion objective (NA 1.45). Dye molecules were photoswitched to the dark state and imaged using a 647-nm laser (MPB Communications); this laser was passed through an acousto-optic tunable filter and introduced through an optical fiber into the back focal plane of the microscope and onto the sample at an intensity of ~2 kW cm^2. A translation stage was used to shift the laser beam toward the edge of the objective so the light reached the sample at incident angles slightly smaller than the critical angle of the glass-water interface. A 405-nm laser was used concurrently with the 647-nm laser to reactivate fluorophores into the emitting state. The power of the 405-nm laser (typical range 0-1 W cm^{-2}) was adjusted during image acquisition so that at any given instant, only a small, optically resolvable fraction of the fluorophores in the sample was in the emitting state. For 3D STORM imaging, a cylindrical lens was inserted into the imaging path so that images of single molecules were elongated in opposite directions for molecules on the proximal and distal sides of the focal plane (Huang et al. 2008). The raw STORM data were analyzed according to previously described methods (Rust, Bates, and Zhuang 2006; Huang et al. 2008). Data were collected at a frame rate of 110 Hz for a total of ~80,000 frames per image. Single and two-color imaging was performed on cells labeled with Alexa Fluor 647 only or Alexa Fluor 647 and CF680 with 647-nm excitation based on a ratiometric detection scheme (Bossi et al. 2008; Testa et al. 2010; Gorur et al. 2017). In the two-color imaging scheme, light emitted from the AF647 and CF680 fluorophores was collected concurrently and split into two light paths using a long pass dichroic mirror (T685lpxr; Chroma). Each light path was projected onto one half of an Andor iXon Ultra 897 EM-CCD camera. Dye assignment was performed by localizing and recording the intensity of each single molecule in each channel. Conventional imaging of 560- and 488-nm dyes was performed immediately prior to STORM imaging using the appropriate laser and filter set. Emission data were collected through the short wavelength reflected path of the aforementioned optical setup and overlaid directly onto the final STORM image.

Selection of clathrin-coated super-resolved structures for image analysis: Clathrin-containing structures were extracted from processed STORM images using a custom MATLAB routine. Briefly, a kernel convolution with a disk of ~80 nm radius was performed on the super-resolved clathrin image channel to accentuate possible clathrin-coated pits. The resulting image

was median filtered, and peaks were detected by sequentially identifying and cropping out regions corresponding to the local image maxima. 310 nm x 310 nm wide square regions centered at these peaks were cropped from all color channels and aligned. Subsequently, we selected super-resolved clathrin coats by visual inspection for further quantitative image analysis based on the following criteria: We excluded clathrin labeled structures for image analysis that looked deformed, that covered almost the entire 310 nm x 310 nm wide square, or that contained small punctuated clathrin structures which were not distinguishable from background noise or small clathrin seeds (Fig. S1 A). Clathrin-coated structures selected for analysis were first inspected to determine whether they appear round-shaped, elliptical-shaped or triangle-shaped in the x-y projected super-resolved image. These images were 3D rendered to determine whether the x-z projection resulted in the typical wider-crescent shape, U-shape or round-shape appearance of the clathrin coat. If we could identify the stereotypical clathrin-coat shapes in both projections, we included the clathrin-coat in the pool for further image analysis. We then classified clathrin coats by manual inspection of DNM2-eGFP^{EN} fluorescence signal intensity into DNM2 negative or positive: When the 3x3 pixel kernel aligned with the super-resolved clathrin-coat was at the same or lower intensity relative to the surrounding pixels, the coat was classified as DNM2 negative (Fig. S4 A and C). When the 3x3 pixel kernel showed a very bright middle and/or a bright pixel in the kernel aligned with the clathrin-coat, the coat was classified as DNM2 positive (Fig. S4 B and D). Second, we assigned the clathrin-coats as being actin negative when the number of localizations in the actin channel in the 310 nm x 310 nm ROI was below 50, since we could not distinguish whether these localizations came from background or emanated from actin (Fig. S4 A and B). Clathrin-coated structures were classified as actin positive when the number of localizations in the actin channel in the 310 nm x 310 nm ROI were above 50 and actin signal overlapped with the clathrin signal.

STORM image data display in figures: Reconstructed super-resolution images were visualized using the "insight" software package and saved in a 'png' file format (Huang et al. 2008). These images were loaded into ImageJ, converted from an RGB image into an 8 bit image, pseudocolored for clathrin = red hot, actin = cyan, and then converted back into an RGB image.

Image analysis of reconstructed clathrin and actin side views: Selected reconstructed super-resolved images of clathrin and actin were treated as digital images for further analysis. A custom-written Jupyter notebook script was used to project reconstructed side views of clathrin and actin onto their x- and z-axis to obtain histograms of the clathrin and actin pixel intensity signals normalized to their respective maximum intensity value (Fig. S1 B and C). From these normalized z-axis and x-axis pixel intensity histograms we read out the height and width of clathrin and actin at the 30th percentile. This process resulted in more robust results than the read out at the full width at half maximum (Fig. S1 B and C).

Actin and clathrin coat height: The z-axis intensity histograms were used to report the actin and clathrin coat heights in the x-z projections. Before extracting the values, a mean filter (50) was run over the histograms to reduce signal fluctuations that interfere with the size measurement (Fig. S1 B and C).

Actin-clathrin overlap calculation: We calculated the total overlap between clathrin and actin using the indices obtained at the upper position of clathrin and lower position of actin at the 30th percentile of the respective z - axis projected intensity histograms (Fig. S1 B). We then reported the overlap relative to the clathrin height in units of percentage.

Clathrin-coat width: We used the 30th percentile of x-axis intensity histogram to report the clathrin coat width in the x-z projection. Before extracting the values, a median filter (100) was run over the histogram to smooth out signal fluctuations that interfere with the correct size determination (Fig. S1 B and C).

Shape index calculation: Shape indices of individual clathrin structures are defined as the ratio between clathrin coat height and clathrin coat width. This value allowed us to sort flat (low shape index) and rounded (high shape index) clathrin coats from each other.

Asymmetry of actin signal around clathrin coat: To evaluate the asymmetry of the spatial actin organization around the clathrin coat, we determined the difference in the positions of the peak actin and clathrin signals on both x-z and y-z projections of our images (Fig. S5 G). We obtained the center of the clathrin coat in nm by rendering the clathrin super-resolved image into a diffraction limited image, as explained in paragraph 'Selection of clathrin-coated super-resolved structures for image analysis'. We first identified the position of the actin maximum intensity in the x-z projection profile and y-z projection profile in nm. Then we measured the distance of these obtained position to the middle position of the clathrin intensity profile. This distance

measurement is proportional to the asymmetry of the actin position with respect to clathrin; namely a low distance corresponds to high symmetry and a high distance corresponds to high asymmetry in the position of the actin signal.

Clathrin coat surface area: We determined the width of clathrin coats in x and y and height in z from the x-z and y-z projections of the reconstructed, super-resolved images. x, y and z values were then used to calculate the coat surface area with the formula of a half ellipsoid by Knud Thompson's approximation:

$$A = \frac{4 \times \pi \times \left(\frac{((z \times x)^{1,6075} + (z \times y)^{1,6075} + (x \times y)^{1,6075})}{3}\right)^{\frac{1}{1,6075}}}{2}.$$

Total internal reflection fluorescence (TIRF) microscopy:TIRF imaging was carried out on a Nikon Eclipse Ti2 inverted microscope with a CFI60 60x Apo TIRF objective and a Hamamatsu Orca-Flash 4.0 V2 sCMOS camera. eGFP and Tag.RFP-T fluorescence were excited using 488 nm and 561 nm lasers and detected using a Chroma HC TIRF Quad Dichroic (C-FL TIRF Ultra Hi S/N 405/488/561/638) and Chroma HC Quad emission filters BP 525/50 and BP600/50, respectively (Bellows Falls, VT). Unless mentioned specifically, channels were acquired sequentially at a 1.2 sec interval and 400ms exposure time over 4.8 minutes to 6 minutes. Real-time acquisition was achieved by a National Instruments (PXI 1033, Austin, TX) controller. The system was controlled with NIS-Elements software and maintained at 37°C by an OkoLab environmental chamber (Burlingame, CA).

Hypo-osmotic media treatment: SK-MEL-2 cells were plated on glass coverslips one day prior to osmotic treatment and imaging: 20,000 cells/ mL were seeded 16h – 24h prior to the experiment on 25 mm round #1.5 glass coverslips that had been cleaned with 70% ethanol (Warner Instruments, 64-0715). Isotonic imaging media contained Dublbecco's Modified Essential Medium and Ham's F-12 medium (DMEM/F12) without phenol red (11039, Thermo Fisher Scientific) with 5% v/v FBS. The media was diluted with an inorganic salt solution containing 10mM $CaCl_2$, 0.3mM $MgCl_2$ and 0.1mM $MgSO_4$ (CMM) to maintain concentrations of critical ions, while obtaining hypo-osmotic conditions by diluting the media containing components such as D-Glucose. 225 mOsm hypotonic imaging media contained 1:4 v/v CMM solution in DMEM/F12, 150 mOsm hypotonic imaging media contained 1:1 v/v CMM solution

in DMEM/F12, and 75 mOsm hypotonic imaging media contained 4:1 v/v CMM solution in DMEM/F12. 5% v/v FBS was present in all hypotonic solutions.

Images of CLTA-TagRFP-T^{EN} and DNM2-eGFP^{EN} fluorescence in SK-MEL-2 cells were acquired first in isotonic media over a course of 4.8 minutes. Subsequently, media was exchanged on the stage to hypotonic media (either 225 mOsm, 150 mOsm or 75 mOsm) and movies were acquired for 4.8 minutes, starting 2 minutes and 10 minutes after media exchange. Media exchange on the stage did not affect CME initiation rates or fluorescence lifetimes beyond the existing experimental intrinsic variability (Fig. S3 A).

CK666 concentration titration: 20,000 SK-MEL-2 cells/ mL were seeded in 8 well chambers 16h – 24h prior to the experiment (80826, ibidi, Fitchburg, WC). A CK666 (SML0006, batch # 0000012761, Sigma Aldrich) stock solution was prepared at 50mM in DMSO and kept at -20 ^{o}C. 25μM, 50μM and 100 μM CK666 and equivalent 0.5% v/v DMSO, 1% v/v DMSO and 2% DMSO v/v solutions for controls were prepared fresh in DMEM/F12 containing 5% FBS and kept at 37°C until used. Cells were first imaged in DMEM/F12 containing 5% FBS solution as a baseline control for 4.8 minutes. Subsequently, imaging solution was exchanged on the microscopy stage to CK666 or DMSO containing imaging solution and another 4.8-minute movie was acquired after 2 minutes of treatment. Each treatment was repeated twice and an area of 1024 pixel x 1024 pixel was used to record 3-6 cells per experiment.

CK666 in combination with hypo-osmotic media: Cells were prepared as for the CK666 concentration titration experiment described above. Solutions of 2% v/v DMSO in DMEM/F12, 100 μM CK666 in DMEM/F12, 2% v/v DMSO in 1:1 v/v CMM solution in DMEM/F12 (150 mOsm hypotonic media) and 100 μM CK666 1:1 v/v CMM solution in DMEM/F12 (150 mOsm hypotonic media) were prepared fresh and kept at 37°C until used. All solutions contained 5% FBS. Cells were first imaged in DMEM/F12-5% FBS solution as a baseline control for 6 minutes. Subsequently, the imaging solution was exchanged on the microscopy stage to the desired experimental solutions and a 6 minute movie was recoded after 4 minutes of incubation.

Image analysis of TIRF live-cell microscopy data: Fluorescent diffraction-limited spots of DNM2-eGFP^{EN} and CLTA-TagRFP-T^{EN} in SK-MEL-2 cells were tracked in each channel over

the course of the movie using the detection and tracking software feature of the cmeAnalysis software package in Matlab (Aguet et al. 2013). Subsequently, we cleaned up the background signal and, based on the x and y positions of associated CLTA-TagRFP-T^{EN} and DNM2-eGFP^{EN} fluorescent tracks, separated them from CLTA-TagRFP-T^{EN} and DNM2-eGFP^{EN} that were not associated with each other, using a custom-written Matlab script (Hong, Cortesio, and Drubin 2015; Ferguson et al. 2016; Dambournet et al. 2018). We obtained fluorescence lifetimes for DNM2-eGFP^{EN} and CLTA-TagRFP-T^{EN} tracks that were associated and not associated with each other and that appeared and disappeared within the duration of a movie. We classified the tracks as "persistent" when they were already present in the first movie frame and lasted longer than the movie.

CME initiation rate and completion rate measurement: We classified tracks as "complete" when they appeared and disappeared over the course of the movie. When we classified tracks as "initiated," they appeared within the course of the movies, excluding in the first frame, and lasted longer than the movie. Initiated tracks include the number of complete tracks, as well. To calculate rates, we used the binary cell mask image that was generated by the CME analysis program in Matlab that highlights the cell area in which particle tracking was performed. ImageJ was then used to calculate the area of the cell from the binary mask image.

Tether pulling experiments using Atomic Force Microscopy: Custom-cut 35-mm glass-bottom dishes (Greiner Bio-One, #627860) were coated with fibronectin (50 ug/mL, Corning #356008) for 30 minutes and washed with DPBS shortly before use. SK-MEL-2 cells were seeded at a density of 0.15-0.20x10^5 cells/ml in DMEM/F12 GlutaMax^{TM} supplement media with 1% FBS and penicillin-streptomycin mix (Gibco^{TM}, #15140-122) in a 37°C humid incubator with 5% CO^2 for 2-4 hours, and used directly for membrane tether pulling experiments. OBL-10 cantilevers (Bruker) were mounted on a CellHesion 200 AFM (Bruker) integrated into an Eclipse Ti inverted light microscope (Nikon), calibrated using thermal noise method and coated with 2.5 mg/ml Concanavalin A (C5275, Sigma) for 1 hour at 30°C. After rinsing the cantilever with DPBS, it was positioned at any location over the cell for tether pulling using brightfield imaging. Approach velocity was set to 1 μm/s, contact force to 100–300 pN, contact time to 300 ms–10 s, and retraction speed to 10 μm/s. After a 10 μm tether was pulled,

the cantilever position was held constant until the moment of tether breakage and at least 2 seconds afterwards. Sampling rate was set to 2000 Hz. After measurements of tether forces in control conditions, an inorganic salt solution containing 10mM $CaCl_2$, 0.3mM $MgCl_2$ and 0.1mM $MgSO_4$ was added to the medium (4:1 v/v) to achieve 75 mOsm hypotonic treatment. Tether forces were measured after media dilution for 2-16 minutes. Tether forces per cell are the average of at least 3 tethers. Cells were not used longer that 1 h for data acquisition. Force-time curves analysis was performed using the JPKSPM Data Processing Software.

Data analysis, statistical analysis and data plotting: For statistical analysis and data plotting, Prism version 7.0e and Jupyter notebook 5.5.0 were used.

Online supplemental material: Fig. S1 gives an overview of clathrin structure selection and parameter extraction of super-resolved clathrin and actin. Representative x-y STORM image projections are shown of super-resolved clathrin, actin and NWASP, corresponding to the images in Fig. 2. In Fig. S2 we present additional data from live cell imaging of SK-MEL-2 cells endogenously expressing CLTA-TagRFP-T^{EN} and DNM2-$eGFP^{EN}$ in hypotonic and isotonic control media. Fig. S3 establishes the CK666 concentration affecting CME in SK-MEL-2 cells and provides additional data on CK666 and concomitant hypotonic media treatment. Fig. S4 shows x-y STORM projections of actin and clathrin with or without a DNM2-$eGFP^{EN}$ diffraction limited fluorescence signal corresponding to x-z projections in Fig. 5. The table shows the statistical difference between clathrin coat surface area when cells are in isotonic vs. 75 mOsm hypotonic media. Fig. S5 provides additional data on the effect of hypotonic media treatment on actin organization and how actin asymmetry was quantified.

References

Aghamohammadzadeh, Soheil, and Kathryn R Ayscough. 2009. “Differential Requirements for Actin during Yeast and Mammalian Endocytosis.” *Nature Cell Biology* 11 (8): 1039–42. https://doi.org/10.1038/ncb1918.

923 Akamatsu, Matthew, Ritvik Vasan, Daniel Serwas, Michael A Ferrin, Padmini Rangamani, and
924 David G Drubin. 2020. “Principles of Self-Organization and Load Adaptation by the Actin
925 Cytoskeleton during Clathrin-Mediated Endocytosis.” Edited by Patricia Bassereau, Vivek
926 Malhotra, Patricia Bassereau, and Alex Mogilner. *ELife* 9: e49840.
927 https://doi.org/10.7554/eLife.49840.
928 Almeida-Souza, Leonardo, Rene A.W. Frank, Javier García-Nafría, Adeline Colussi, Nushan
929 Gunawardana, Christopher M. Johnson, Minmin Yu, et al. 2018. “A Flat BAR Protein
930 Promotes Actin Polymerization at the Base of Clathrin-Coated Pits.” *Cell* 174 (2): 325-
931 337.e14. https://doi.org/10.1016/j.cell.2018.05.020.
932 Avinoam, Ori, Martin Schorb, Carsten J. Beese, John A. G. Briggs, and Marko Kaksonen. 2015.
933 “Endocytic Sites Mature by Continuous Bending and Remodeling of the Clathrin Coat,”
934 June, 1–5. papers3://publication/uuid/231D4B9E-8B87-42F4-A0F3-D3A15874D418.
935 Berro, Julien, Vladimir Sirotkin, and Thomas D. Pollard. 2010. “Mathematical Modeling of
936 Endocytic Actin Patch Kinetics in Fission Yeast: Disassembly Requires Release of Actin
937 Filament Fragments.” *Molecular Biology of the Cell* 21 (2905–2915).
938 Bossi, Mariano, Jonas Fo, Vladimir N Belov, Vadim P Boyarskiy, Alexander Egner, Christian
939 Eggeling, Andreas Scho, Stefan W Hell, and Rebecca Medda. 2008. “Multicolor Far-Field
940 Fluorescence Nanoscopy through Isolated Detection.” *Nano Lett.* 8: 2463–2468.
941 https://doi.org/10.1021/nl801471d.
942 Boulant, Steeve, Comert Kural, Jean-Christophe Zeeh, Florent Ubelmann, and Tomas
943 Kirchhausen. 2011. “Actin Dynamics Counteract Membrane Tension during Clathrin-
944 Mediated Endocytosis.” *Nature Cell Biology* 13 (9): 1124–31.
945 http://dx.doi.org/10.1038/ncb2307.

946 Bucher, Delia, Felix Frey, Kem A. Sochacki, Susann Kummer, Jan Philip Bergeest, William J.
947 Godinez, Hans Georg Kräusslich, et al. 2018. "Clathrin-Adaptor Ratio and Membrane
948 Tension Regulate the Flat-To-Curved Transition of the Clathrin Coat during Endocytosis."
949 *Nature Communications* 9 (1). https://doi.org/10.1038/s41467-018-03533-0.
950 Buser, Christopher, and David G. Drubin. 2013. "Ultrastructural Imaging of Endocytic Sites in
951 Saccharomyces Cerevisiae by Transmission Electron Microscopy and Immunolabeling."
952 *Microscopy and Microanalysis* 19 (2): 381–92.
953 https://doi.org/10.1017/S1431927612014304.
954 Carlsson, Anders E., and Philip V. Bayly. 2014. "Force Generation by Endocytic Actin Patches
955 in Budding Yeast." *Biophysical Journal* 106 (8): 1596–1606.
956 https://doi.org/10.1016/j.bpj.2014.02.035.
957 Carroll, S. Y., H. E. M. Stimpson, J. Weinberg, C. P. Toret, Y. Sun, and D. G. Drubin. 2012.
958 "Analysis of Yeast Endocytic Site Formation and Maturation through a Regulatory
959 Transition Point." *Molecular Biology of the Cell* 23 (4): 657–68.
960 https://doi.org/10.1091/mbc.e11-02-0108.
961 Clainche, Christophe Le, Barbara S. Pauly, Claire X. Zhang, Åsa E.Y. Engqvist-Goldstein,
962 Kimberley Cunningham, and David G. Drubin. 2007. "A Hip1R-Cortactin Complex
963 Negatively Regulates Actin Assembly Associated with Endocytosis." *EMBO Journal* 26
964 (5): 1199–1210. https://doi.org/10.1038/sj.emboj.7601576.
965 Clarke, Nicholas I., and Stephen J. Royle. 2018. "FerriTag Is a New Genetically-Encoded
966 Inducible Tag for Correlative Light-Electron Microscopy." *Nature Communications* 9 (1):
967 1–10. https://doi.org/10.1038/s41467-018-04993-0.
968 Collins, Agnieszka, Anthony Warrington, Kenneth A Taylor, and Tatyana Svitkina. 2011.

969 "Structural Organization of the Actin Cytoskeleton at Sites of Clathrin-Mediated
970 Endocytosis." *Current Biology* 21 (14): 1167–75.
971 http://www.cell.com/article/S0960982211006063/fulltext.
972 Dambournet, Daphné, Kem A. Sochacki, Aaron T. Cheng, Matthew Akamatsu, Justin W.
973 Taraska, Dirk Hockemeyer, and David G. Drubin. 2018. "Genome-Edited Human Stem
974 Cells Expressing Fluorescently Labeled Endocytic Markers Allow Quantitative Analysis of
975 Clathrin-Mediated Endocytosis during Differentiation." *Journal of Cell Biology*.
976 https://doi.org/10.1083/jcb.201710084.
977 Diz-Muñoz, Alba, Daniel A Fletcher, and Orion D Weiner. 2013. "Use the Force: Membrane
978 Tension as an Organizer of Cell Shape and Motility." *Trends in Cell Biology* 23 (2): 47–53.
979 http://dx.doi.org/10.1016/j.tcb.2012.09.006.
980 Diz-Muñoz, Alba, Kevin Thurley, Sana Chintamen, Steven J Altschuler, Lani F Wu, Daniel A
981 Fletcher, and Orion D Weiner. 2016. "Membrane Tension Acts Through PLD2 and
982 MTORC2 to Limit Actin Network Assembly During Neutrophil Migration." Edited by
983 Michael Sixt. *PLoS Biology* 14 (6): e1002474.
984 http://dx.plos.org/10.1371/journal.pbio.1002474.
985 Dmitrieff, Serge, and François Nédélec. 2015. "Membrane Mechanics of Endocytosis in Cells
986 with Turgor." *PLoS Computational Biology* 11 (10): 1–15.
987 https://doi.org/10.1371/journal.pcbi.1004538.
988 Doyon, Jeffrey B, Bryan Zeitler, Jackie Cheng, Aaron T Cheng, Jennifer M Cherone, Yolanda
989 Santiago, Andrew H Lee, et al. 2011. "Rapid and Efficient Clathrin-Mediated Endocytosis
990 Revealed in Genome-Edited Mammalian Cells." *Nature Cell Biology* 13 (3): 331–37.
991 http://www.nature.com/doifinder/10.1038/ncb2175.

992 Engqvist-Goldstein, A E, R A Warren, M M Kessels, J H Keen, J Heuser, and D G Drubin. 2001.
993 "The Actin-Binding Protein Hip1R Associates with Clathrin during Early Stages of
994 Endocytosis and Promotes Clathrin Assembly in Vitro." *The Journal of Cell Biology* 154
995 (6): 1209–23. http://www.jcb.org/lookup/doi/10.1083/jcb.200106089.
996 Ferguson, Joshua P., Nathan M. Willy, Spencer P. Heidotting, Scott D. Huber, Matthew J.
997 Webber, and Comert Kural. 2016. "Deciphering Dynamics of Clathrin-Mediated
998 Endocytosis in a Living Organism." *Journal of Cell Biology* 214 (3): 347–58.
999 https://doi.org/10.1083/jcb.201604128.
1000 Ferguson, Joshua P, Scott D Huber, Nathan M Willy, Esra Aygün, Sevde Goker, Tugba Atabey,
1001 and Comert Kural. 2017. "Mechanoregulation of Clathrin-Mediated Endocytosis." *Journal*
1002 *of Cell Science* 130 (21): 3631 LP – 3636. https://doi.org/10.1242/jcs.205930.
1003 Ferguson, Shawn M, Shawn Ferguson, Andrea Raimondi, Summer Paradise, Hongying Shen,
1004 Kumi Mesaki, Agnes Ferguson, et al. 2009. "Coordinated Actions of Actin and BAR
1005 Proteins Upstream of Dynamin at Endocytic Clathrin-Coated Pits." *Developmental Cell* 17
1006 (6): 811–22. http://linkinghub.elsevier.com/retrieve/pii/S1534580709004791.
1007 Fujimoto, L M, R Roth, J E Heuser, and S L Schmid. 2000. "Actin Assembly Plays a Variable,
1008 but Not Obligatory Role in Receptor-Mediated Endocytosis in Mammalian Cells." *Traffic*
1009 *(Copenhagen, Denmark)* 1 (2): 161–71. http://www.ncbi.nlm.nih.gov/pubmed/11208096.
1010 Gorur, Amita, Lin Yuan, Samuel J Kenny, Satoshi Baba, Ke Xu, and Randy Schekman. 2017.
1011 "COPII-Coated Membranes Function as Transport Carriers of Intracellular Procollagen I."
1012 *Journal of Cell Biology* 216 (6): 1745–59. https://doi.org/10.1083/jcb.201702135.
1013 Grassart, Alexandre, Aaron T. Cheng, Sun Hae Hong, Fan Zhang, Nathan Zenzer, Yongmei
1014 Feng, David M. Briner, Gregory D. Davis, Dmitry Malkov, and David G. Drubin. 2014.

1015 "Actin and Dynamin2 Dynamics and Interplay during Clathrin-Mediated Endocytosis."
1016 *Journal of Cell Biology* 205 (5): 721–35. https://doi.org/10.1083/jcb.201403041.
1017 Guo, Siyang, Olga S. Sokolova, Johnson Chung, Shae Padrick, Jeff Gelles, and Bruce L. Goode.
1018 2018. "Abp1 Promotes Arp2/3 Complex-Dependent Actin Nucleation and Stabilizes Branch
1019 Junctions by Antagonizing GMF." *Nature Communications* 9 (1).
1020 https://doi.org/10.1038/s41467-018-05260-y.
1021 Hassinger, Julian E, George Oster, David G Drubin, and Padmini Rangamani. 2017. "Design
1022 Principles for Robust Vesiculation in Clathrin-Mediated Endocytosis." *Proceedings of the*
1023 *National Academy of Sciences of the United States of America* 114 (7): E1118–27.
1024 http://www.pnas.org/lookup/doi/10.1073/pnas.1617705114.
1025 Hauser, Meghan, Rui Yan, Wan Li, Nicole A Repina, David V Schaffer, Ke Xu, Meghan
1026 Hauser, et al. 2018. "The Spectrin-Actin-Based Periodic Cytoskeleton as a Conserved
1027 Nanoscale Scaffold and Ruler of the Neural Stem Cell Lineage Article The Spectrin-Actin-
1028 Based Periodic Cytoskeleton as a Conserved Nanoscale Scaffold and Ruler of the Neural
1029 Stem Cell Lineage," 1512–22. https://doi.org/10.1016/j.celrep.2018.07.005.
1030 Helgeson, Luke A., and Brad J. Nolen. 2013. "Mechanism of Synergistic Activation of Arp2/3
1031 Complex by Cortactin and N-WASP." *ELife* 2013 (2): 1–26.
1032 https://doi.org/10.7554/eLife.00884.
1033 Hetrick, Byron, Min Suk Han, Luke A Helgeson, and Brad J Nolen. 2013. "Small Molecules
1034 CK-666 and CK-869 Inhibit Actin-Related Protein 2/3 Complex by Blocking an Activating
1035 Conformational Change." *Chemistry and Biology* 20 (5): 701–12.
1036 https://doi.org/https://doi.org/10.1016/j.chembiol.2013.03.019.
1037 Hong, Sun Hae, Christa L Cortesio, and David G Drubin. 2015. "Machine-Learning-Based

Analysis in Genome-Edited Cells Reveals the Efficiency of Clathrin-Mediated Endocytosis." *Cell Reports* 12 (12): 2121–30. http://linkinghub.elsevier.com/retrieve/pii/S221112471500933X.

Huang, Bo, Wenqin Wang, Mark Bates, and Xiaowei Zhuang. 2008. "Three-Dimensional Super-Resolution Reconstruction Microscopy." *Science* 319 (February): 810–13. https://doi.org/10.1126/science.1153529.

Idrissi, Fatima Zahra, A. Blasco, A. Espinal, and M. I. Geli. 2012. "Ultrastructural Dynamics of Proteins Involved in Endocytic Budding." *Proceedings of the National Academy of Sciences* 109 (39): E2587–94. https://doi.org/10.1073/pnas.1202789109.

Idrissi, Fatima Zahra, Helga Grötsch, Isabel M. Fernández-Golbano, Cristina Presciatto-Baschong, Howard Riezman, and María Isabel Geli. 2008. "Distinct Acto/Myosin-I Structures Associate with Endocytic Profiles at the Plasma Membrane." *Journal of Cell Biology* 180 (6): 1219–32. https://doi.org/10.1083/jcb.200708060.

Kaksonen, Marko, and Aurelien Roux. 2018. "Mechanisms of Clathrin-Mediated Endocytosis." *Nature Reviews Molecular Cell Biology* 19 (5): 313–26. https://doi.org/10.1038/nrm.2017.132.

Kaksonen, Marko, Yidi Sun, and David G. Drubin. 2003. "A Pathway for Association of Receptors, Adaptors, and Actin during Endocytic Internalization." *Cell* 115 (4): 475–87. https://doi.org/10.1016/S0092-8674(03)00883-3.

Kaur, Satdip, Andrew B Fielding, Gisela Gassner, Nicholas J Carter, and Stephen J Royle. 2014. "An Unmet Actin Requirement Explains the Mitotic Inhibition of Clathrin-Mediated Endocytosis." *ELife* 3 (February): e00829. https://elifesciences.org/articles/00829.

Kukulski, Wanda, Martin Schorb, Marko Kaksonen, and John A G Briggs. 2012. "Plasma

Membrane Reshaping during Endocytosis Is Revealed by Time-Resolved Electron Tomography." *Cell* 150 (3): 508–20. https://doi.org/10.1016/j.cell.2012.05.046.

Li, Yiming, Markus Mund, Philipp Hoess, Joran Deschamps, Ulf Matti, Bianca Nijmeijer, Vilma Jimenez Sabinina, Jan Ellenberg, Ingmar Schoen, and Jonas Ries. 2018. "Real-Time 3D Single-Molecule Localization Using Experimental Point Spread Functions." *Nature Methods* 15 (5): 367–69. https://doi.org/10.1038/nmeth.4661.

Liu, Jian, Yidi Sun, David G. Drubin, and George F. Oster. 2009. "The Mechanochemistry of Endocytosis." *PLoS Biology* 7 (9). https://doi.org/10.1371/journal.pbio.1000204.

Merrifield, Christien J., David Perrais, and David Zenisek. 2005. "Coupling between Clathrin-Coated-Pit Invagination, Cortactin Recruitment, and Membrane Scission Observed in Live Cells." *Cell* 121 (4): 593–606. https://doi.org/10.1016/j.cell.2005.03.015.

Messa, Mirko, Rubén Fernández-Busnadiego, Elizabeth Wen Sun, Hong Chen, Heather Czapla, Kristie Wrasman, Yumei Wu, et al. 2014. "Epsin Deficiency Impairs Endocytosis by Stalling the Actin-Dependent Invagination of Endocytic Clathrin-Coated Pits." *ELife* 3 (August): 4116–25. http://elifesciences.org/lookup/doi/10.7554/eLife.03311.

Mulholland, Jon, Amie Wong, David Botstein, Daphne Preuss, Anne Moon, and David Drubin. 1994. "Ultrastructure of the Yeast Actin Cytoskeleton and Its Association with the Plasma Membrane." *Journal of Cell Biology* 125 (2): 381–91. https://doi.org/10.1083/jcb.125.2.381.

Mund, Markus, Johannes Albertus van der Beek, Joran Deschamps, Serge Dmitrieff, Philipp Hoess, Jooske Louise Monster, Andrea Picco, François Nédélec, Marko Kaksonen, and Jonas Ries. 2018. "Systematic Nanoscale Analysis of Endocytosis Links Efficient Vesicle Formation to Patterned Actin Nucleation." *Cell* 174 (4): 884-896.e17.

https://doi.org/10.1016/j.cell.2018.06.032.

Nickaeen, Masoud, Julien Berro, Thomas D Pollard, Boris M Slepchenko, and Alex Mogilner. 2019. "Actin Assembly Produces Sufficient Forces for Endocytosis in Yeast." https://doi.org/10.1091/mbc.E19-01-0059.

Picco, Andrea, Markus Mund, Jonas Ries, François Nédélec, and Marko Kaksonen. 2015. "Visualizing the Functional Architecture of the Endocytic Machinery." *ELife* 4: 1–29. https://doi.org/10.7554/elife.04535.

Pinyol, Roser, Akvile Haeckel, Anett Ritter, Britta Qualmann, and Michael Manfred Kessels. 2007. "Regulation of N-WASP and the Arp2/3 Complex by Abp1 Controls Neuronal Morphology." *PLoS ONE* 2 (5). https://doi.org/10.1371/journal.pone.0000400.

Pollard, Thomas D. 2007. "Regulation of Actin Filament Assembly by Arp2/3 Complex and Formins." *Annual Review of Biophysics and Biomolecular Structure* 36 (1): 451–77. https://doi.org/10.1146/annurev.biophys.35.040405.101936.

Pontes, Bruno, Pascale Monzo, and Nils C. Gauthier. 2017. "Membrane Tension: A Challenging but Universal Physical Parameter in Cell Biology." *Seminars in Cell and Developmental Biology* 71: 30–41. https://doi.org/10.1016/j.semcdb.2017.08.030.

Raucher, D, and M P Sheetz. 1999. "Membrane Expansion Increases Endocytosis Rate during Mitosis." *The Journal of Cell Biology* 144 (3): 497–506.

Rust, Michael J., Mark Bates, and Xiaowei Zhuang. 2006. "Sub-Diffraction-Limit Imaging by Stochastic Optical Reconstruction Microscopy (STORM)." *Nature Methods* 3 (10): 793–95. https://doi.org/10.1038/nmeth929.

Sahl, Steffen J, Stefan W Hell, and Stefan Jakobs. 2017. "Fluorescence Nanoscopy in Cell Biology." *Nature Reviews Molecular Cell Biology* 18 (11): 685–701.

https://doi.org/10.1038/nrm.2017.71.

Saleem, Mohammed, Sandrine Morlot, Annika Hohendahl, John Manzi, Martin Lenz, and Aurélien Roux. 2015. "A Balance between Membrane Elasticity and Polymerization Energy Sets the Shape of Spherical Clathrin Coats." *Nature Communications* 6. https://doi.org/10.1038/ncomms7249.

Schöneberg, Johannes, Martin Lehmann, Alexander Ullrich, York Posor, Wen Ting Lo, Gregor Lichtner, Jan Schmoranzer, Volker Haucke, and Frank Noé. 2017. "Lipid-Mediated PX-BAR Domain Recruitment Couples Local Membrane Constriction to Endocytic Vesicle Fission." *Nature Communications* 8 (May). https://doi.org/10.1038/ncomms15873.

Sigal, Yaron M, Ruobo Zhou, and Xiaowei Zhuang. 2018. "Visualizing and Discovering Cellular Structures with Super-Resolution Microscopy." *Science* 361 (6405): 880 LP – 887. https://doi.org/10.1126/science.aau1044.

Skruzny, Michal, Thorsten Brach, Rodolfo Ciuffa, Sofia Rybina, Malte Wachsmuth, and Marko Kaksonen. 2012. "Molecular Basis for Coupling the Plasma Membrane to the Actin Cytoskeleton during Clathrin-Mediated Endocytosis." *Proceedings of the National Academy of Sciences of the United States of America* 109 (38): E2533-42. http://www.pnas.org/cgi/doi/10.1073/pnas.1207011109.

Skruzny, Michal, Ambroise Desfosses, Simone Prinz, Svetlana O. Dodonova, Anna Gieras, Charlotte Uetrecht, Arjen J. Jakobi, et al. 2015. "An Organized Co-Assembly of Clathrin Adaptors Is Essential for Endocytosis." *Developmental Cell* 33 (2): 150–62. https://doi.org/10.1016/j.devcel.2015.02.023.

Sochacki, Kem A., and Justin W. Taraska. 2019. "From Flat to Curved Clathrin: Controlling a Plastic Ratchet." *Trends in Cell Biology* 29 (3): 241–56.

https://doi.org/10.1016/j.tcb.2018.12.002.

Sochacki, Kem A, Andrea M Dickey, Marie-Paule Strub, and Justin W Taraska. 2017. "Endocytic Proteins Are Partitioned at the Edge of the Clathrin Lattice in Mammalian Cells." *Nature Cell Biology* 19 (4): 352–61. http://www.nature.com/doifinder/10.1038/ncb3498.

Sun, Yidi, Johannes Schöneberg, Xuyan Chen, Tommy Jiang, Charlotte Kaplan, Ke Xu, Thomas D Pollard, and David G Drubin. 2019. "Direct Comparison of Clathrin-Mediated Endocytosis in Budding and Fission Yeast Reveals Conserved and Evolvable Features" 3.

Testa, Ilaria, Christian A. Wurm, Rebecca Medda, Ellen Rothermel, Claas Von Middendorf, Jonas Fölling, Stefan Jakobs, Andreas Schönle, Stefan W. Hell, and Christian Eggeling. 2010. "Multicolor Fluorescence Nanoscopy in Fixed and Living Cells by Exciting Conventional Fluorophores with a Single Wavelength." *Biophysical Journal* 99 (8): 2686–94. https://doi.org/10.1016/j.bpj.2010.08.012.

Wang, Xinxin, and Anders E. Carlsson. 2017. "A Master Equation Approach to Actin Polymerization Applied to Endocytosis in Yeast." *PLoS Computational Biology* 13 (12): 1–15. https://doi.org/10.1371/journal.pcbi.1005901.

Willy, N. M., J. P. Ferguson, S. D. Huber, S. P. Heidotting, E. Aygün, S. A. Wurm, E. Johnston-Halperin, M. G. Poirier, and C. Kural. 2017. "Membrane Mechanics Govern Spatiotemporal Heterogeneity of Endocytic Clathrin Coat Dynamics." *Molecular Biology of the Cell* 28 (24): 3480–88. https://doi.org/10.1091/mbc.e17-05-0282.

Willy, N M, J P Ferguson, Salih Silahli, Cemal Cakez, Farah Hasan, Henry C Chang, Alex Travesset, et al. 2019. "Endocytic Clathrin Coats Develop Curvature at Early Stages of Their Formation." *BioRxiv*, January, 715219. https://doi.org/10.1101/715219.

Wojcik, Michal, Margaret Hauser, Wan Li, Seonah Moon, and Ke Xu. 2015. "Graphene-Enabled Electron Microscopy and Correlated Super-Resolution Microscopy of Wet Cells." *Nature Communications* 6 (1): 7384. https://doi.org/10.1038/ncomms8384.

Xu, Ke, Hazen P. Babcock, and Xiaowei Zhuang. 2012. "Dual-Objective STORM Reveals Three-Dimensional Filament Organization in the Actin Cytoskeleton." *Nature Methods* 9 (2): 185–88. https://doi.org/10.1038/nmeth.1841.

Xu, Ke, Guisheng Zhong, and Xiaowei Zhuang. 2013. "Actin, Spectrin, and Associated Proteins Form a Periodic Cytoskeletal Structure in Axons." *Science* 339 (6118): 452 LP – 456. https://doi.org/10.1126/science.1232251.

Yarar, Defne, Clare M Waterman-Storer, and Sandra L Schmid. 2005. "A Dynamic Actin Cytoskeleton Functions at Multiple Stages of Clathrin-Mediated Endocytosis." *Molecular Biology of the Cell* 16 (2): 964–75. http://www.molbiolcell.org/content/16/2/964.full.

Author contributions

C. Kaplan and D.G. Drubin conceived the study and experiments. C. Kaplan performed live cell data acquisition, SRM data analysis and live cell data analysis. Sam J. Kenny, Shirley Chen and Ke Xu performed SRM, super-resolution data reconstruction and supervised SRM imaging. Johannes Schöneberg supported the SRM data analysis. Ewa M. Sitarska and Alba Diz-Muñoz performed membrane tether pulling experiments by atomic force microscopy, data analysis and supervised AFM tether pulling experiments. C. Kaplan and D.G. Drubin wrote the manuscript with feedbacks from other authors.

Acknowledgments: CK was funded by the German research foundation (DFG KA4305/1-1). DGD was funded by NIH grant R35GM118149. KX was funded by NSF under CHE-1554717 and the Pew Biomedical Scholars Award. ADM was funded by the European Molecular Biology Laboratory (EMBL), the Human Frontiers Science Program (HFSP) grant number RGY0073/2018 and the Deutsche Forschungsgemeinschaft (DFG) grant numbers DI 2205/2-1 and DI 2205/3-1.

ES was funded by the EMBL and the Joachim Herz Stiftung Add-on Fellowship for Interdisciplinary Science. We thank Yidi Sun, Matt Akamatsu, Padmini Rangamani and Ross T.A. Pedersen for critical reading and discussions on the manuscript. We thank Sungmin Son and Daniel A. Fletcher for valuable input and discussion on the manuscript.

Abbreviations:

CME Clathrin-mediated endocytosis
CCV Clathrin coated vesicles
CCS clathrin coated structure
CCP Clathrin coated pits
SI shape index

Figure legends

Figure 1: Simultaneous two-color, three-dimensional stochastic optical reconstruction microscopy (2c-3D STORM) resolves clathrin structures highly connected to the actin cortex. (A) Current model of actin (blue) organization at clathrin structures (red) based on platinum-replica EM data. The schematic shows clathrin coat progression from a shallow membrane invagination to a fully formed membrane vesicle and organization of the associated actin network. Perspectives representing the x-y projection (top profile) and the x-z projection (side profile) are shown. **(B)** STORM image of clathrin coats on the ventral surface of an SK-MEL-2 cell immunolabeled with the CF-680 antibody. **(C)** STORM field corresponding to (B) showing the actin cytoskeleton labeled with phalloidin-AF647. **(D)** Merged clathrin and actin STORM images from (B) and (C). Orange squares are areas shown in Figure 1E. **(B) – (D)** Scale bars: 5 μm. **(E)** Magnification of highlighted areas 1 and 2 in Figure 1D. STORM images of clathrin coats (left) and clathrin-coats merged with actin (right). Orange squares identify clathrin coats of interest. Scale bars are 250 nm. **(F)** STORM images of clathrin coats and actin showing the x-z projection generated by three-dimensional rendering of insets 1 and 2 from (E). The white dashed line shows the orientation to the plasma membrane. Color code scale bar shows the height in the z-dimension for actin. Scale bars: 100 nm.

Figure 2: The actin network is nucleated from the base of endocytic pits and its assembly is not coupled to clathrin coat progression. (A) Left schematic shows range of shape indexes (SI) calculated from height to width ratios that classify the endocytic stages of clathrin coats (red) into early (SI < 0.7), intermediate (0.7 < SI > 0.9) and late (0.9 < SI). STORM images show x-z projections of representative clathrin-coats (red) with different actin (cyan) coverages of clathrin.

The SI for each clathrin coat is given in the lower right corner of each panel. (**B)** Shape index of clathrin coats from all three endocytic stages in (A) is plotted against the percentage of clathrin covered by actin (actin coverage >0.05%). The percentage of clathrin coats with below 50% actin coverage and above 50% of actin coverage is shown in the upper left and right corner. **(C)** The schematic shows the clathrin coat in the side profile and actin either at the tip, covering the clathrin coat completely, or at the base of the clathrin coat. The dashed black lines indicate the average position of actin and clathrin in the z-dimension. "D_z" represents the resulting distance when subtracting the actin average from clathrin average position. Difference of average actin position to average clathrin position plotted against the percentage of actin covering clathrin (clathrin coverage >0.05%, n = 719). The inset predicts how the data plot would look when actin grows from the clathrin coat tip (red line) or when actin grows from the clathrin coat base. **(D**) - **(E)** Schematic of clathrin coat side profiles shows N-WASP localization. Merged STORM images show spatial localization of N-WASP-AF647 (rainbow) at clathrin coats (red) in x-z projections. **(D)** N-WASP is localized at the base of clathrin coats. **(E)** N-WASP is localized all over clathrin coats. All scale bars in (A), (D) and (E) are 100 nm.

Figure 3: Clathrin-mediated endocytosis mechanosensitivity. (A) Schematic shows actin organization in CME when cells are in isotonic media (left). Hypotonic media (right) causes water influx and stretches the cell membrane. However, how actin assembly at CME sites is affected was not known. **(B)** Kymographs show lifetimes of CLTA-TagRFP-T^{EN} (magenta) and DNM2-eGFP^{EN} (green) as viewed by total-internal reflection microscopy. Imaging was performed for 4.8 min. SK-MEL-2 cells were imaged in isotonic media, or 2 min or 10 min after hypotonic media exchange. **(C)** and **(D)** Normalized cumulative distribution fluorescence track

lifetime data are shown for CLTA-TagRFP-T^{EN} associated with (C) or not associated with DNM2-eGFP^{EN} (D). Control cumulative distribution curve is red, 2 min cumulative distribution curve is violet and 10 min cumulative distribution curve in orange. **(E)** and **(F)** Normalized cumulative distribution fluorescence track lifetime data for DNM2-eGFP^{EN} associated with (E) or not associated with CLTA-TagRFP-T^{EN} (F). Control cumulative distribution curve is light green, 2 min cumulative distribution curve is dark green and 10 min cumulative distribution curve in blue. **(C)** – **(F)** Experiment was repeated 4 times. Lifetimes were recorded in isotonic media (n = 8 cells) as well as 2 min (n = 8 cells) and 10 min (n = 9 cells) after 75 mOsm hypotonic media exchange. **(G)** Table shows the CLTA-TagRFP-T^{EN} lifetimes when associated with or not associated with DNM2-eGFP^{EN} and the corresponding statistics. **(H)** Table shows the DNM2-eGFP^{EN} lifetimes when associated with or not associated with CLTA-TagRFP-T^{EN} and the corresponding statistics. **(G)** and **(H)** The Kolmogorov-Smirnov statistical test was used. **(I)** Plots represent CME initiation rate for the lifetimes in (C), CME completion rate for the lifetimes in (C) and percentage of persistent tracks over the course of the movie for the lifetimes in (C). **(J)** Mean membrane tether values are plotted for measurements from cells in isotonic media (n = 18) or in 75 mOsm hypotonic media (n = 17). Mean values were obtained by pulling at least 3 tethers from each cell. Round symbols in the plotted 75 mOsm data represent mean tether values from 2 min to 10 min after hypotonic media exchange. Rectangular symbols represent mean tether values obtained between 10 min and 16 min after hypotonic media exchange. **(I)** and **(J)** Bars in plots show mean with SD. The Mann-Whitney statistical test was used.

Figure 4: Arp2/3-mediated actin polymerization importance during CME increases under elevated membrane tension. (A) Kymographs show dynamics of CLTA-TagRFP-T^{EN}

(magenta) and DNM2-eGFP^{EN} (green) imaged by total-internal reflection microscopy for 6 min. SK-MEL-2 cells were imaged first in isotonic media. The media was then exchanged to either 150 mOsm hypotonic media, 100μM CK666 in isotonic media or 100μM CK666 in 150 mOsm hypotonic media, respectively. Images were collected 4 min after changing media. **(B)** Normalized cumulative fluorescence lifetime distribution data for CLTA-TagRFP-T^{EN} associated with DNM2-eGFP^{EN}. Shown are the lifetime curves and statistics for cells cultured in isotonic media before exchange to the indicated experimental media conditions (T = 0). Color code shows the pretreatment control conditions for the treatment in (C). **(C)** Normalized fluorescence track lifetime cumulative distribution data for CLTA-TagRFP-T^{EN} associated with DNM2-eGFP^{EN} after exchange to media containing 2% v/v DMSO in isotonic media (yellow), 2% v/v DMSO in 150 mOsm hypotonic media (green), 150 mOsm hypotonic media (magenta), 100μM CK666 in both isotonic media (light blue) and 150 mOsm hypotonic media (dark blue) (T = 4 min after media exchange). (**D)** Normalized cumulative fluorescence lifetime distribution for pretreatment control data as in (B) except for DNM2-eGFP^{EN} associated with CLTA-TagRFP-T^{EN}. **(E)** Normalized fluorescence lifetime cumulative distribution data as in (C) except for DNM2-eGFP^{EN} associated with CLTA-TagRFP-T^{EN} under the different treatment conditions. **(B)** – **(E)** Right tables show statistics for the normalized distribution functions. Kolmogorov-Smirnov statistical test was used. **(F)** Representative STORM images of immunolabeled clathrin-coated structures. Upper panel shows the x-y projections and lower panel the corresponding x-z projections. Scale bars: 100 nm. **(G)** Clathrin coat heights when cells where treated with only 2% v/v DMSO, 100μM CK666 in isotonic media and 100μM CK666 in 150 mOsm hypotonic media. Clathrin coat images for quantitative analysis were collected from at least 3 cells for each condition. Statistics are given in Figure S3 E. Mann-Whitney statistical test was used.

Figure 5: Super-resolved clathrin coats organized into an endocytic timeline via their shape index, the DNM2-eGFP^{EN} fluorescent signal and actin association. (A), (B), (D) and (E) Schematics show side profiles of clathrin coats (red) and their association with DNM2 (green puncta) and actin (blue bar). Clathrin coats were quantified via their height to width ratio into early (SI < 0.9) and late (SI > 0.9) endocytic stages. Nine hundred and ninety-two clathrin coats were selected from 6 cells acquired in three independent dSTROM experiments to quantify their association with DNM2-eGFP^{EN} and super-resolved actin. **(A)** The image panel shows examples of x-z STORM projection images of early (n = 85) and late (n = 118) clathrin coats without significant presence of DNM2-eGFP^{EN} or actin. The white dashed line locates the plasma membrane. The image row below shows actin (cyan) in the AF647 channel. The third row of images shows the merged clathrin and actin STORM images. **(B)** Same organization of super-resolved clathrin, actin and merged image as in (A). These early (n = 31) and late (n = 22) clathrin coats are associated with DNM2-eGFP^{EN}, but not with actin. **(C)** Schematic of clathrin coats combines the information about coats without and with DNM2-eGFP^{EN} from (A) and (B) and organizes a timeline of early coats without DNM2-eGFP^{EN}, intermediate coats with DNM2-eGFP^{EN}, coats undergoing membrane fission with DNM2-eGFP^{EN} and late coats after fission without DNM2-eGFP^{EN}. **(D)** Same organization of super-resolved clathrin, actin and merged image as in (A). These early (n = 167) and late (n = 202) clathrin coats are not associated with DNM2-eGFP^{EN}, but are associated with actin. **(E)** Same organization of super-resolved clathrin, actin and merged image as in (A). These early (n = 221) and late (n = 156) clathrin coats are associated with DNM2-eGFP^{EN} and actin. **(F)** Schematic of clathrin coats combines the information about coats with actin in combination without and with a DNM2-eGFP^{EN} signal

from (D) and (E). Clathrin coats are organized into a timeline of being early in endocytosis without DNM2-eGFP^{EN}, intermediate in endocytosis with DNM2-eGFP^{EN}, in the membrane fission stage with DNM2-eGFP^{EN} and being late after fission without DNM2-eGFP^{EN}.

Figure 6: Effects of elevated membrane tension on clathrin coat surface area. (A) – (D) Clathrin coat surface area is plotted in the early, intermediate, membrane fission and late endocytic stages for coats lacking actin under **(A)** isotonic media conditions, **(B)** lacking actin under 75 mOsm hypotonic media conditions, **(C)** with actin under isotonic media conditions, **(D)** and with actin under 75 mOsm hypotonic media conditions. **(A) – (D)** Bars show mean with standard deviation. Mann-Whitney statistical test was used.

Figure 7: Actin organization at CME sites adapts to elevated membrane tension. (A) Schematic shows actin organization at CME sites when cells reside in isotonic media (left cell) and after media is exchanged to hypotonic media (right cell). Hypotonic media causes water influx and stretches the cell membrane. As a consequence, the actin network grows higher, resulting in larger coverage of clathrin. **(B)** Plotted are actin heights in nm at clathrin coats measured from STORM x-z projections. Average actin height, SD, number of data points and p-values are listed in Table 1. **(C)** Percentage of clathrin covered by actin in STORM x-z projection images from the same dataset in (B) (actin coverage > 1% plotted). Average percentage, SD and number of data points are listed in Table 1. **(B) – (C)** Clathrin coats are classified as early (SI < 0.9) or late coats (SI > 0.9) based on their height to width ratio (SI) and as DNM2-eGFP^{EN} positive or negative, and classified into early, intermediate, membrane fission and late stages. Bars show mean with standard deviation. Mann-Whitney statistical test was used

in (B). **(D) – (E)** Schematic shows adaptation of actin organization at early and late stage clathrin coats to hypotonic media treatment. MT = membrane tension. Corresponding representative STORM images show clathrin (red) and actin (cyan) in x-z projections. Event number in data set is given in the lower right corner. All scale bars are 100 nm. **(F) – (G)** Actin height in nm from (B) is plotted against clathrin coverage by actin from (C) in percentage from early and late clathrin coats. Grey dots and the grey regression line represent the data set from cells treated with isotonic media and black dots and black regression line represent the data set from cells treated with 75 mOsm media. **(H)** Schematic shows that the distance of the actin signal maximum (cyan) to the center of the clathrin coat (red) increases with asymmetric actin organization. Plot shows distances of the maximum actin signal from the clathrin coat's center in respective x-z and y-z projections. Early clathrin coats: N = 301, intermediate clathrin coats N = 353, clathrin coats at membrane fission N = 256, and late clathrin coats N = 402. **(I)** Schematic shows distance of the actin signal maximum to the center of the clathrin coat to represent asymmetric actin organization. Plot shows distances of the maximum actin signal from the clathrin coat's center in respective x-z projection and y-z projection under 75 mOsm hypotonic media. Mann-Whitney statistical test was used in **(B)**, **(H)** and **(I)**. **(B), (C), (F) – (H)** Actin heights at clathrin coats in isotonic media were analyzed from the same dataset as in Figure 2. Three independent dSTROM experiments with cells in isotonic (N = 6) and 75 mOsm hyptonic media (N = 7) were performed. **(B)**, **(C)**, **(H)** and **(I)** Bars in plot show mean and SD.

Figure 8: Adaptive actin force generating mechanism counteracts elevated membrane tension to ensure robust CME progression. The model proposes three scenarios in which membrane tension is low, intermediate and high, and how CME is accomplished efficiently by

an adaptive actin network organization. Black arrows indicate actin forces exerted orthogonal and parallel to the membrane invagination.

Table 1: Statistics for clathrin coat surface area. Table provides average clathrin coat surface area in nm^2 over the course of CME under normal and 75 mOsm hypotonic media conditions, without and with actin present. Mann-Whitney statistical test compares the clathrin coat surface area between the different clathrin coat stages when actin is lacking and when actin is present.

Table 2: Statistics for actin height and coverage of clathrin coats. Table provides average actin height in nm and average percentage of clathrin covered by actin over the course of CME under normal and 75 mOsm hypotonic media conditions. Statistical test: Mann-Whitney.

Figure 1

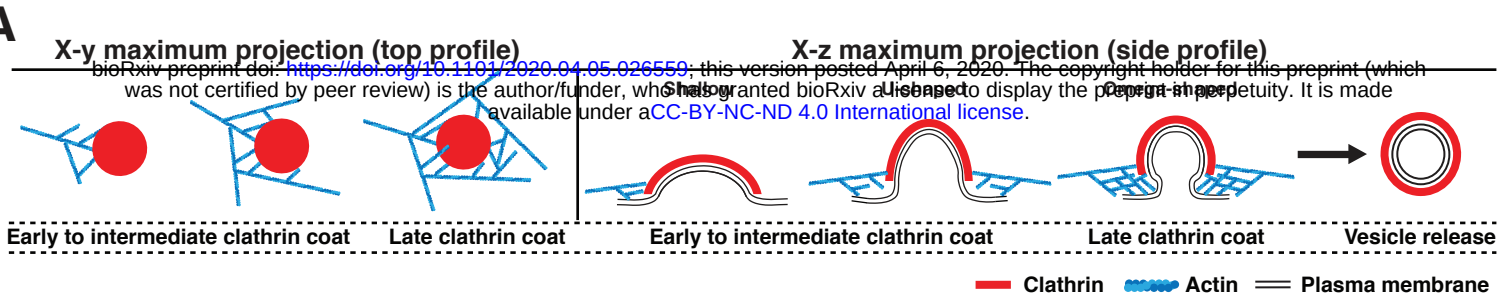

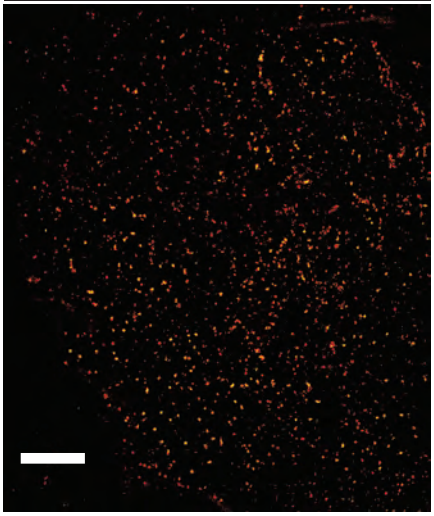

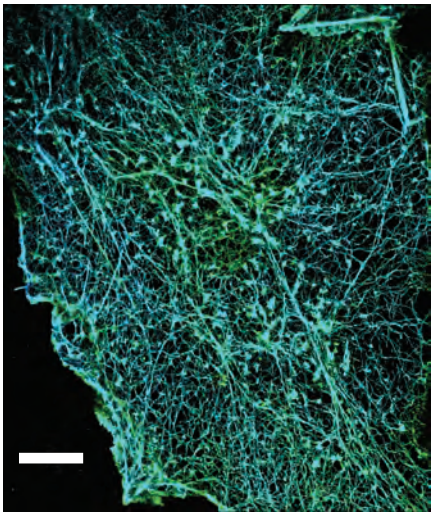

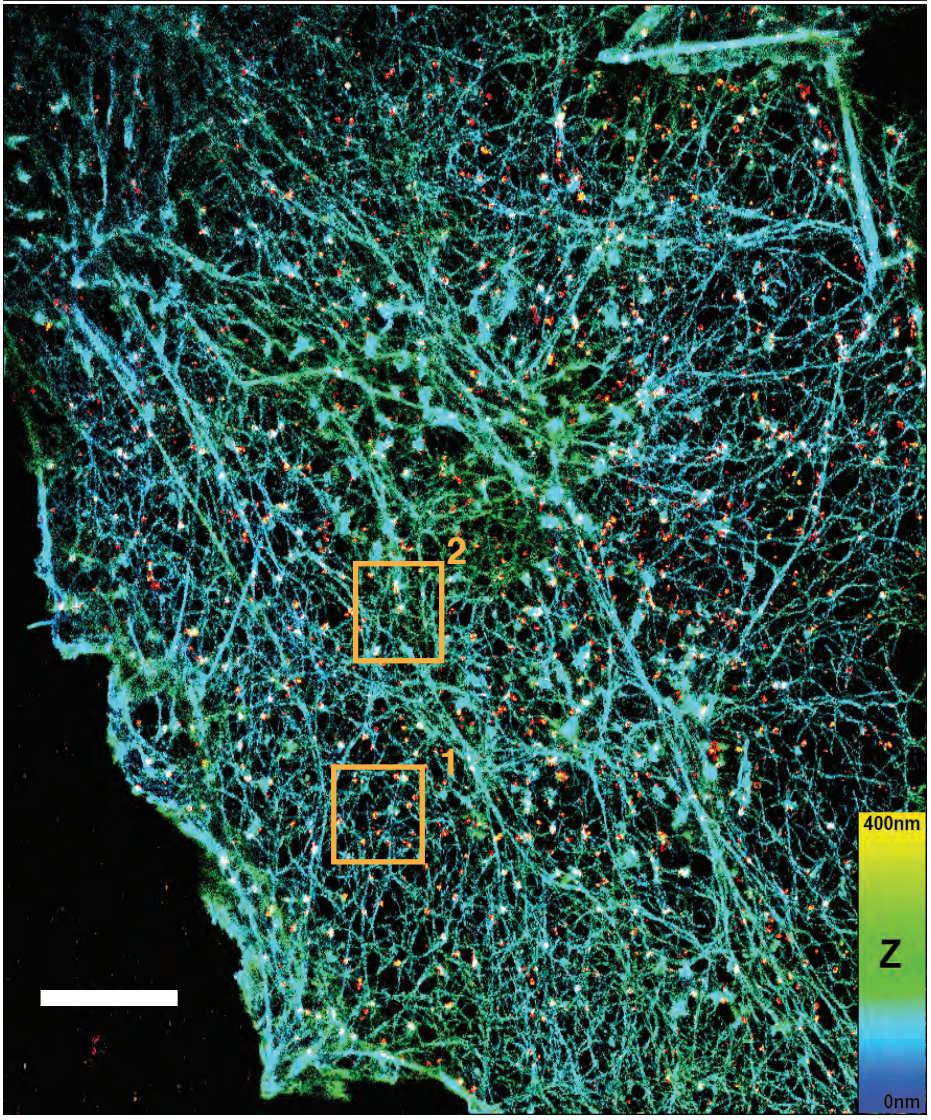

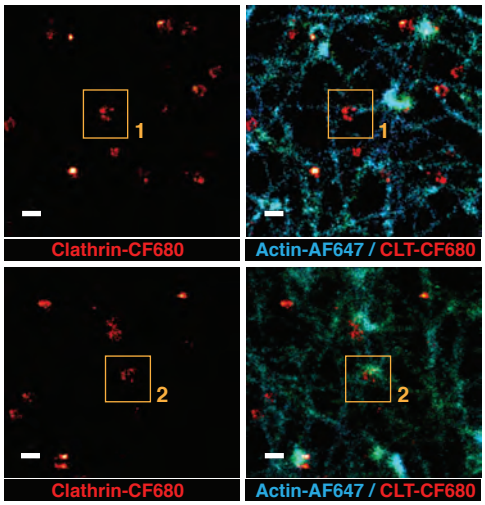

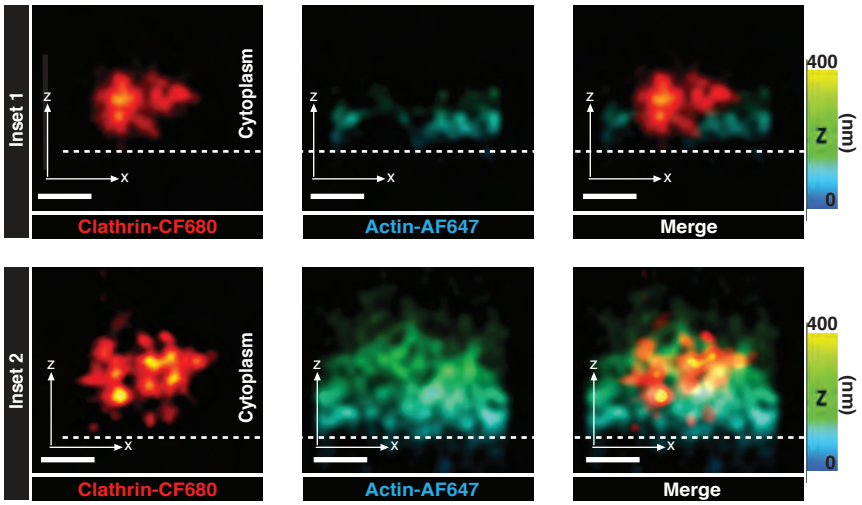

Figure 2

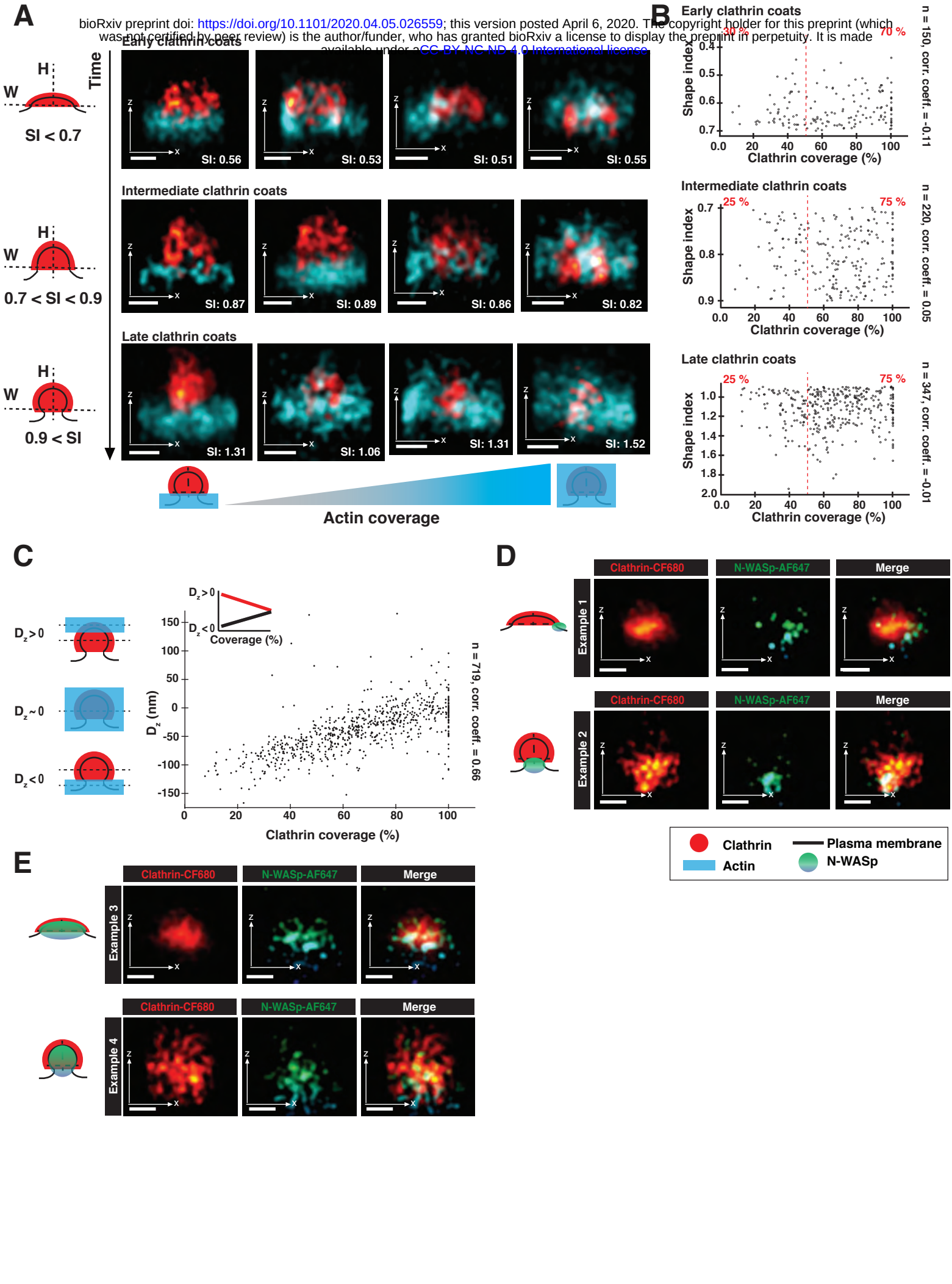

Figure 3

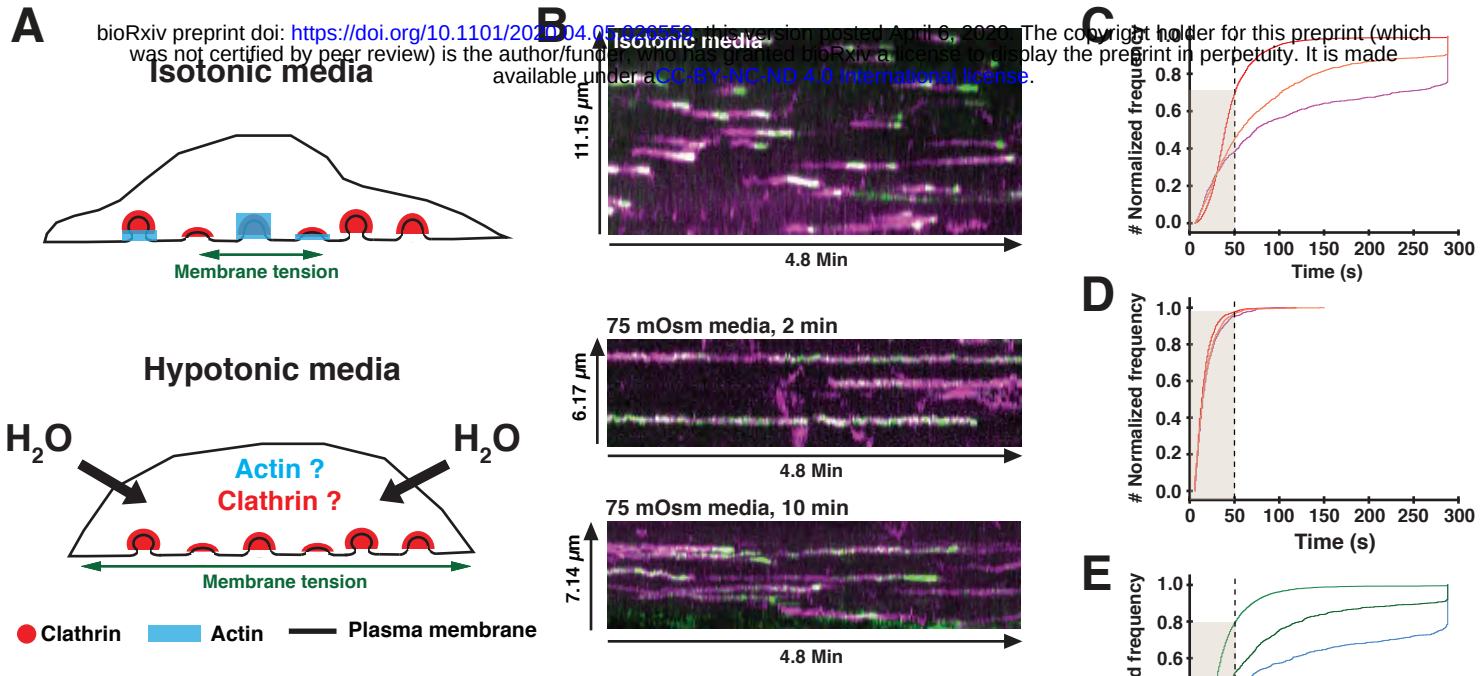

G

	DNM2 - associated				CLT only			
	Mean (s)	SD (s)	N. tracks	p-value to cntrl	Mean (s)	SD (s)	N. tracks	p-value to cntrl
Isotonic media	47.0	32.4	3760		16.8	11.8	1517	
75 mOsm media, 2 min	128.4	111.9	918	3.12E-10	19.6	14.7	742	0.0027
75mOsm media, 10 min	90.7	90.8	1153	9.16E-69	18.7	14.3	954	0.0112

H

	CLT - associated				DNM2 only			
	Mean (s)	SD (s)	N. tracks	p-value to cntrl	Mean (s)	SD (s)	N. tracks	p-value to cntrl
Isotonic media	38.8	32.1	3760		18.9	12.3	1182	
75 mOsm media, 2 min	125.1	111.5	918	5.02E-10	23.3	16.4	1312	3.56E-10
75 mOsm media, 10 min	82.2	83.0	1153	2.59E-64	22.5	17.1	2000	4.92E-08

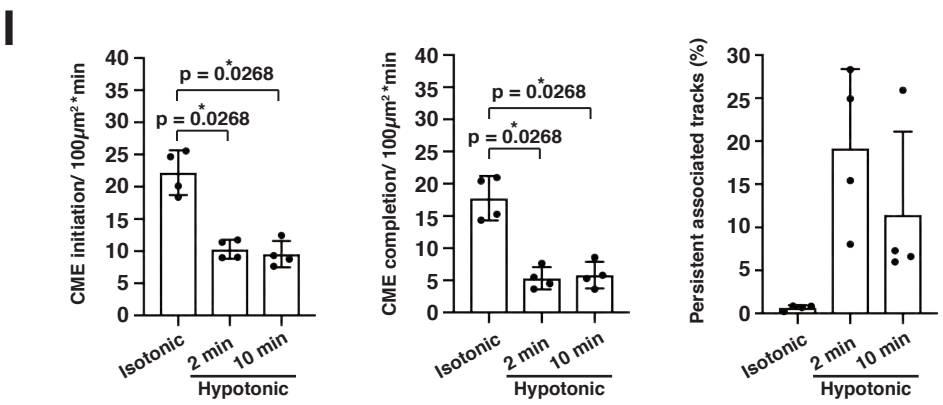

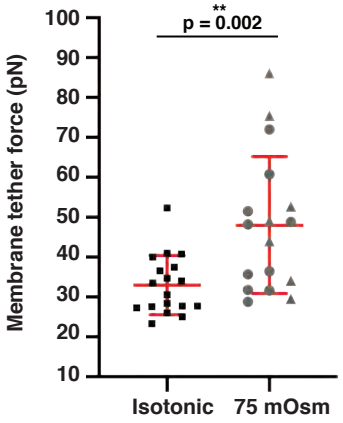

Figure 4

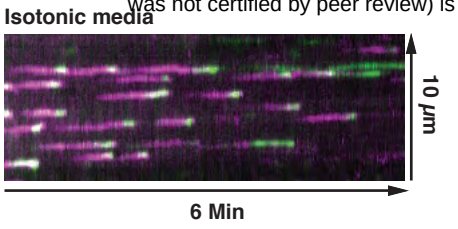

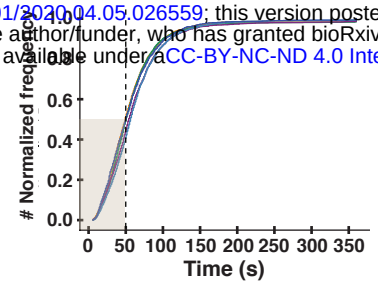

CLTA-tagRFP.t, associated

Pre-treatment to	Mean (s)	SD (s)	N. tracks	N. cells	p-value to DMSO
DMSO	59.0	47.2	2378	10	
DMSO + 150 mOsmo	61.5	52.8	4345	12	0.093
150 mOsm	65.4	53.9	2173	9	3.88E-06
100 μM CK666	64.8	46.0	4219	10	1.18E-14
100 μM CK666 + 150 mOsm	59.1	45.4	1405	9	0.902

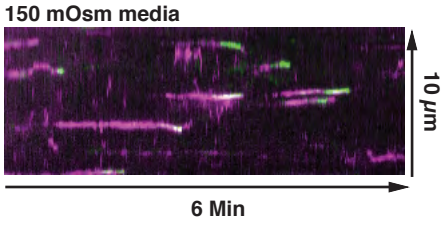

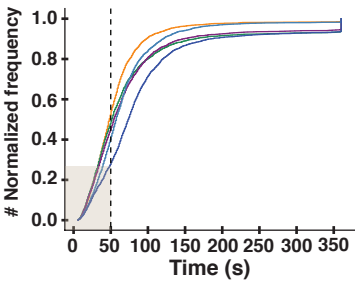

CLTA-tagRFP.t, associated

Treatment	Mean (s)	SD (s)	N. tracks	N. cells	p-value to DMSO
DMSO	59.0	51.9	3028	10	
DMSO + 150 mOsm	80.2	87.4	2286	10	2.13E-13
150 mOsm	79.1	82.0	2762	8	7.15E-20
100 μM CK666	69.5	56.4	3124	10	7.46E25
100 μM CK666 + 150 mOsm	96.3	85.5	2783	10	1.12E-119

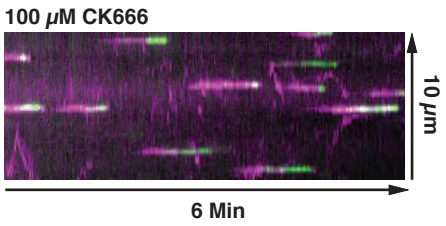

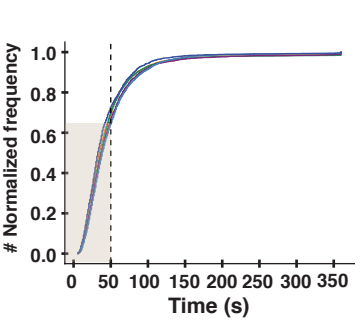

DNM2-eGFP, associated

Pre-treatment to	Mean (s)	SD (s)	N. tracks	N. cells	p-value to DMSO
DMSO	46.7	45.9	2378	10	
DMSO + 150 mOsm	49.5	51.7	4345	12	0.004
150 mOsm	51.1	51.5	2173	9	0.001
100 μM CK666	50.3	43.3	4219	10	2.57E-09
100 μM CK666 + 150 mOsm	44.0	41.4	1405	9	0.094

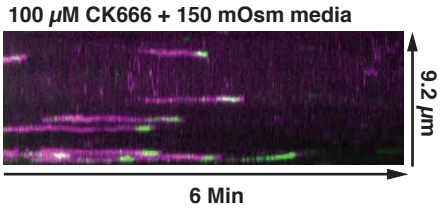

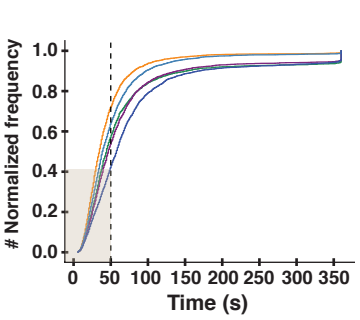

DNM2-eGFP, associated

Treatment	Mean (s)	SD (s)	N. tracks	N. cells	p-value to DMSO
DMSO	46.9	48.8	3028	10	
DMSO + 150 mOsmo	73.5	86.4	2286	10	4.27E-26
150 mOsm	72.5	81.2	2762	8	3.51E-44
100 μM CK666	54.2	54.4	3124	10	8.39E-11
100 μM CK666 + 150 mOsmo	83.5	85.3	2783	10	1.94E-115

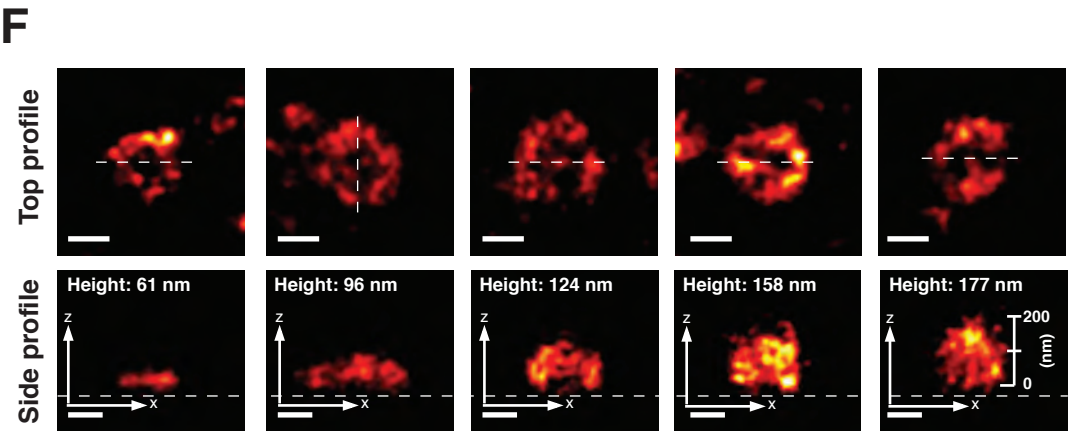

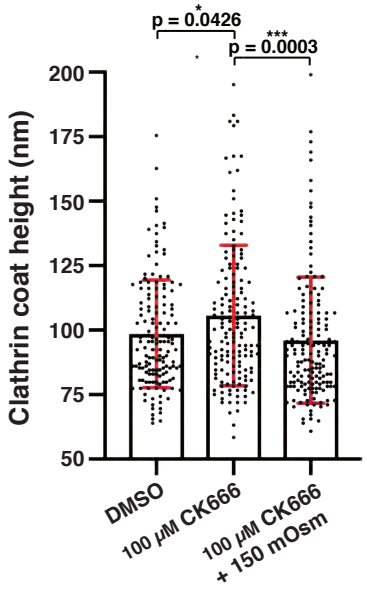

Figure 5

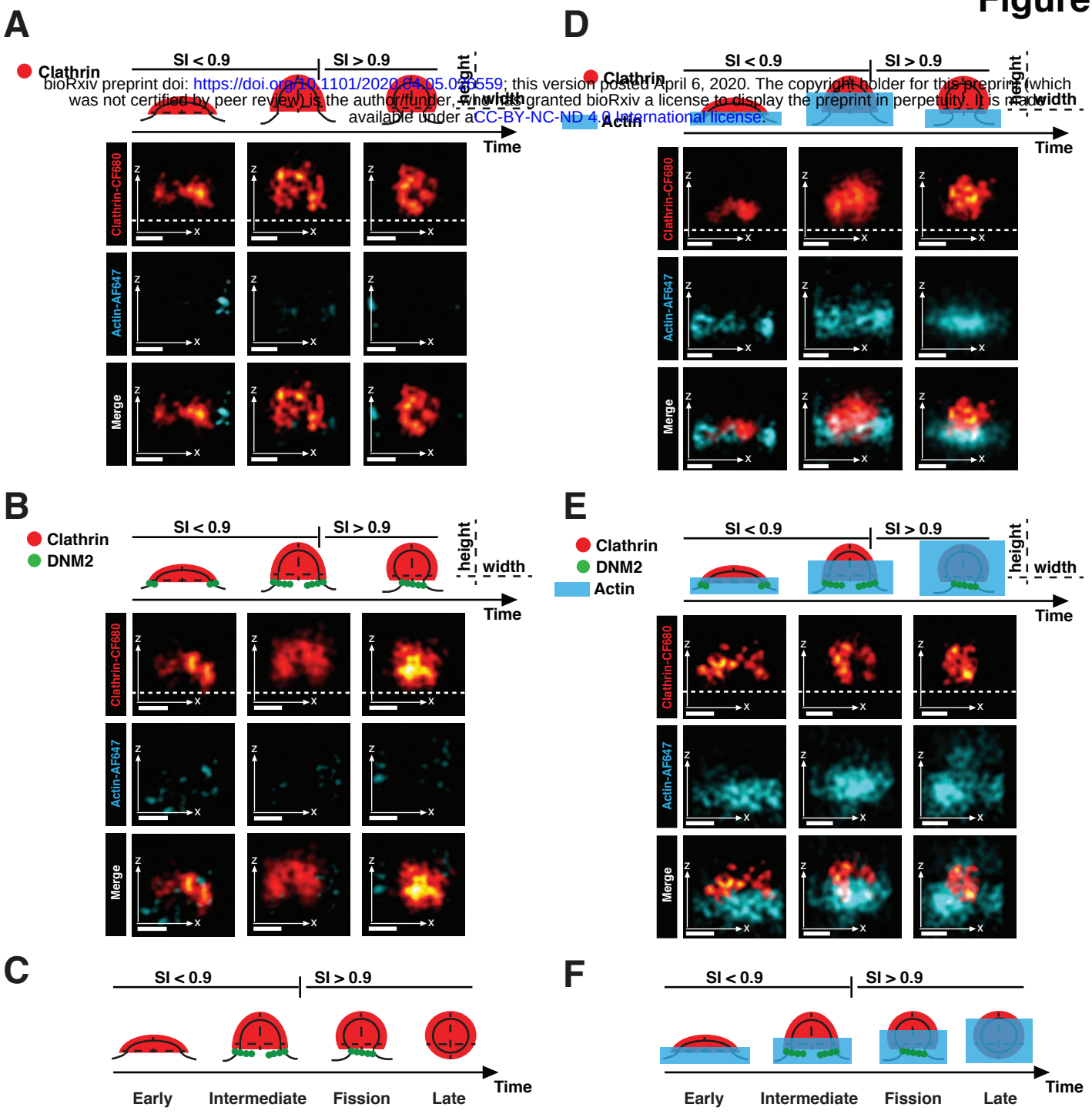

Figure 6

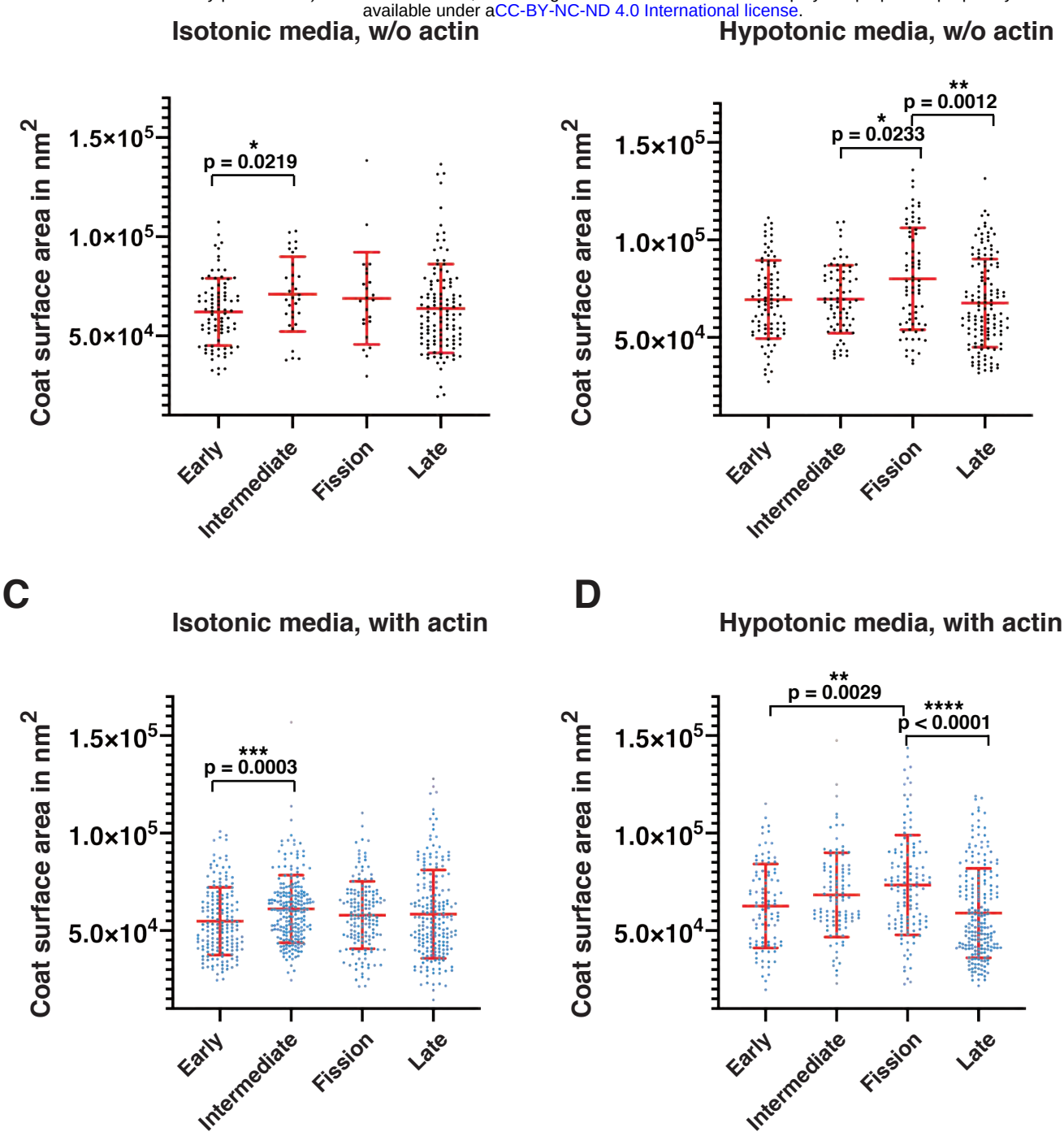

Figure 7

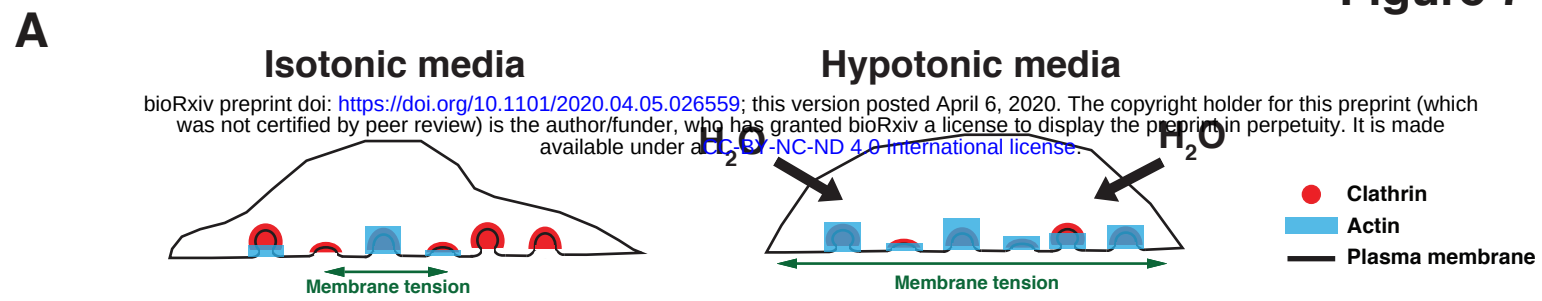

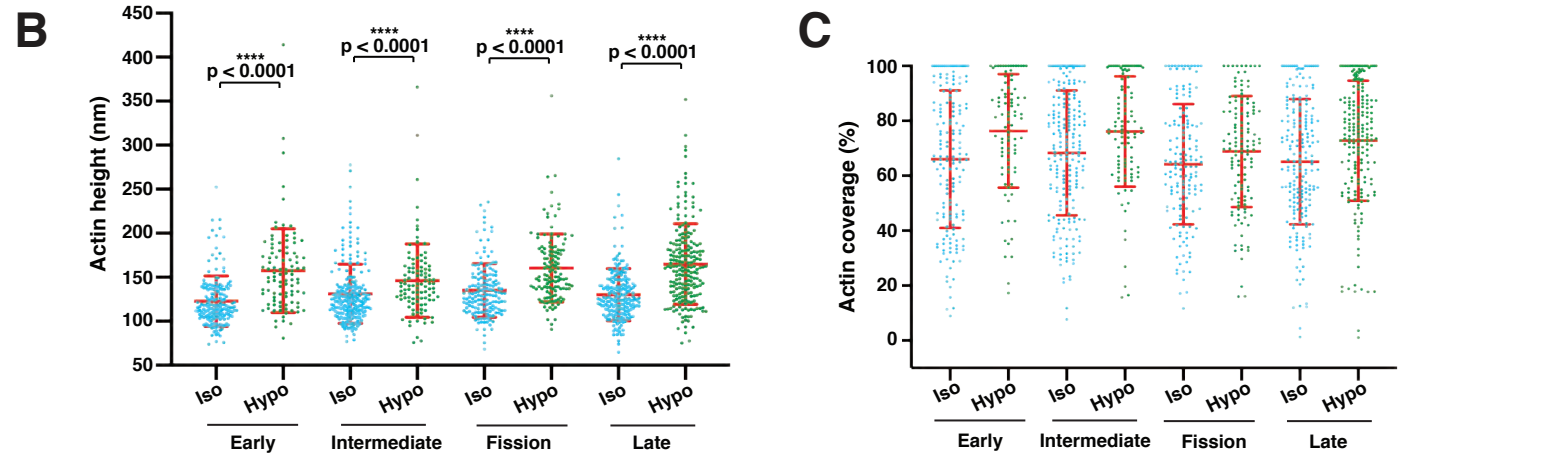

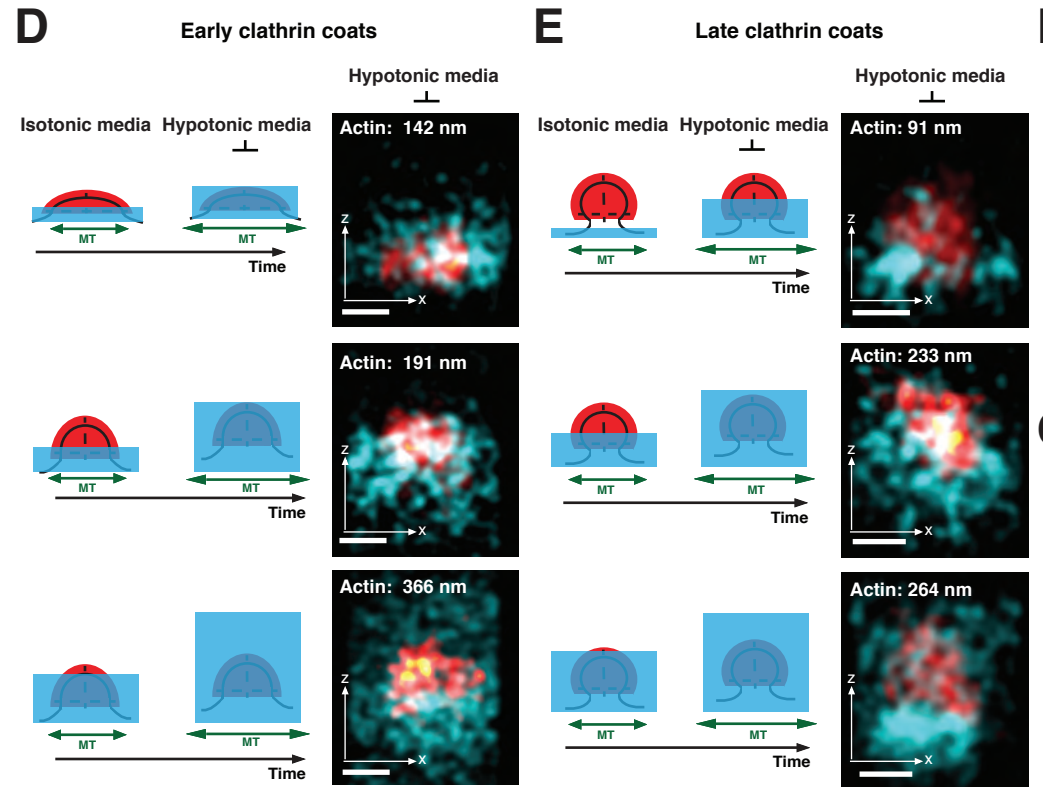

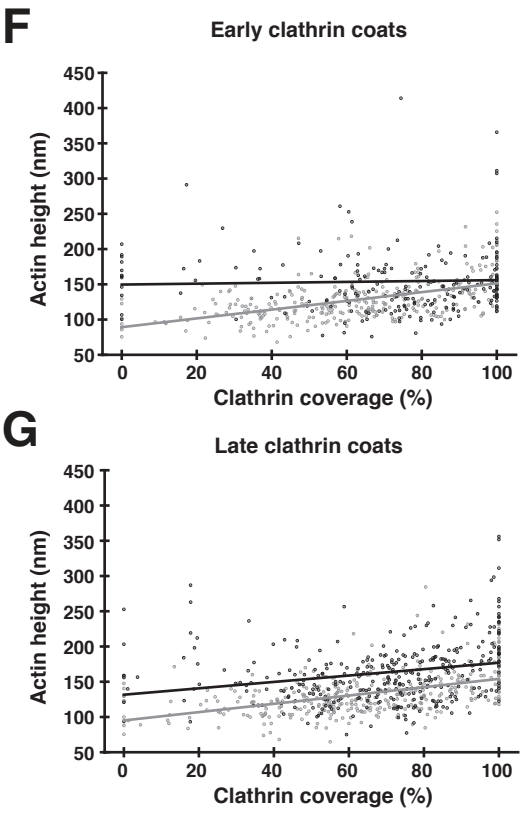

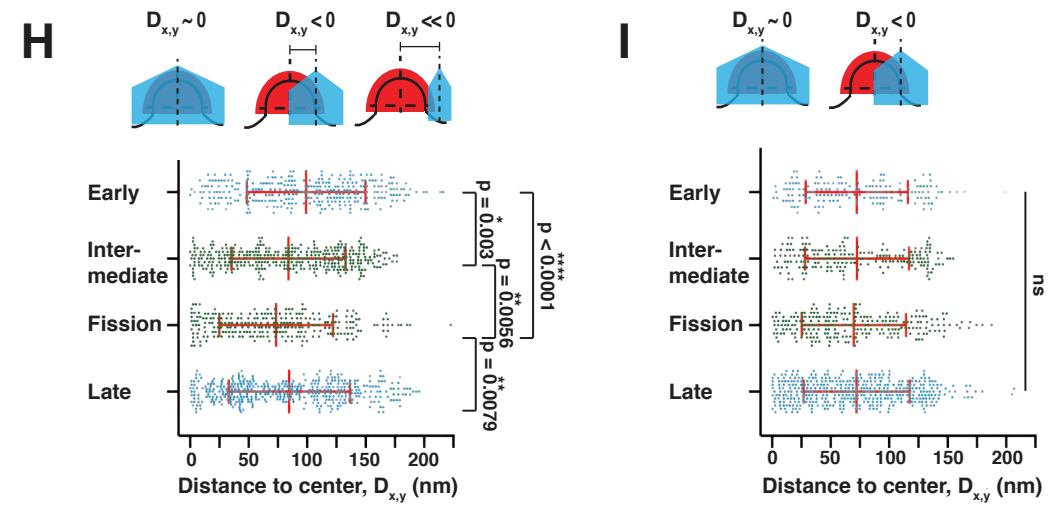

Figure 8

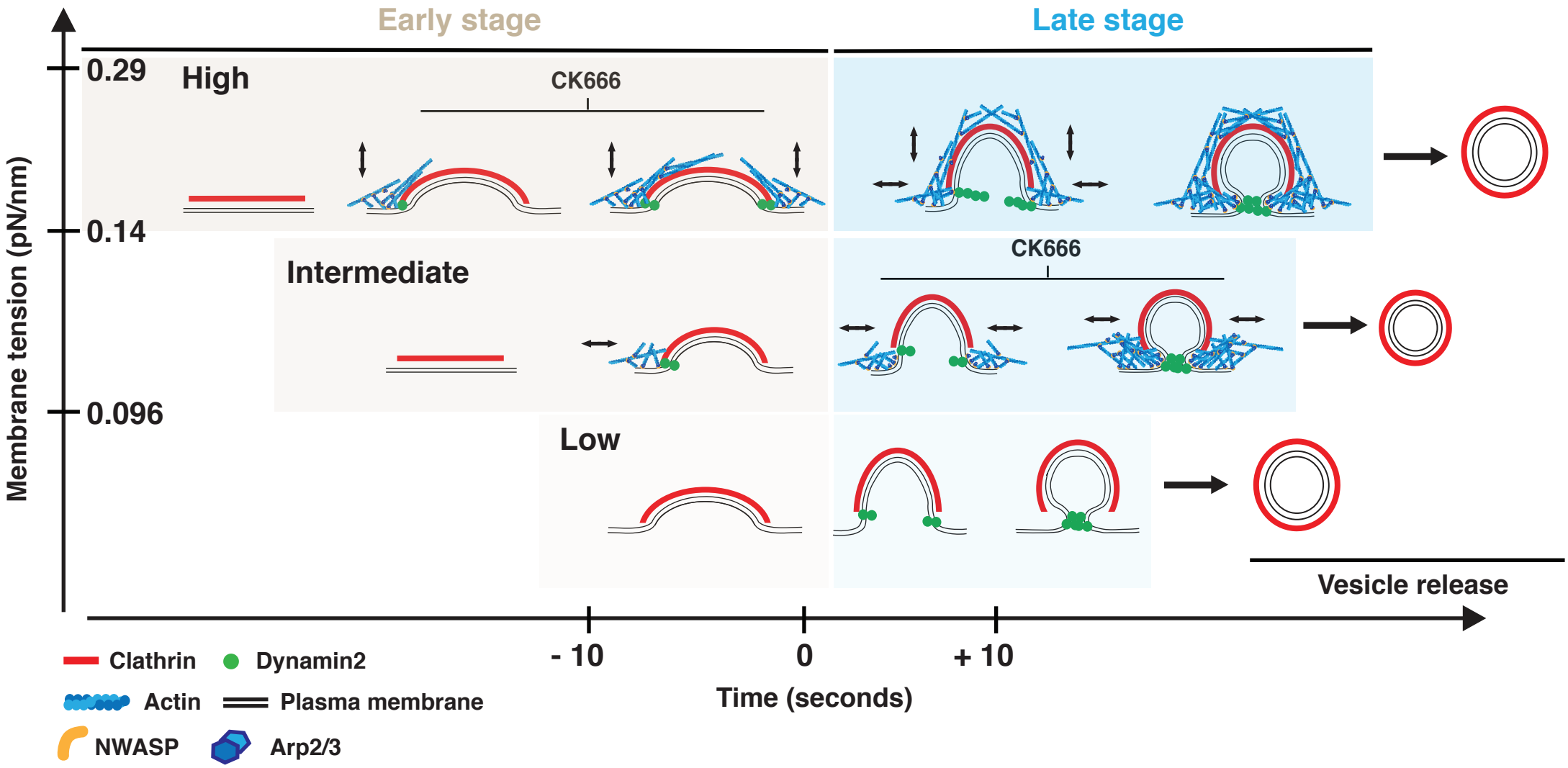
Early stage
Late stage
0.29
0.14
0.096
Membrane tension (pN/nm)
High
CK666
Intermediate
CK666
Low
Vesicle release
- 10
0
+ 10
Time (seconds)
Clathrin
Dynamin2
Actin
Plasma membrane
NWASP
Arp2/3

Figure S1: Representative examples of ambiguous clathrin data, overview of 3D measurement methods for super-resolved clathrin and actin, and representative x-y projections.

(A) Representative examples of immunolabeled clathrin structures that cannot be identified as individual clathrin coated events. dSTORM images show x-y projection of clathrin structures. First two columns show structures that do not show a clear round or elliptical shape. Third image column shows clathrin structures that extend over the entire region of interest. Fourth image column shows very small punctate structures. **(B)** Illustration of method to obtain actin and clathrin height and extent of overlap from super-resolved CCP images. x-z projection of a merged dSTORM image of clathrin and actin with its corresponding normalized pixel intensity histogram projected onto the z-axis. The black line marks the 30th percentile of the z height histogram, which we used to calculate the height of clathrin and actin. We found that this metric, the "full z width at 30th percentile max," was more reliable than the full width at half max. These raw intensity profiles are noisy based on the image quality, which depends on the fluorescent labeling quality of the target structure. Without filtering of the profile, the measured height of clathrin and actin are underestimated. Numbers correspond to positions used to calculate height (in z) of clathrin (1. and 2.) and actin (4. and 5.) and their average positions (3. and 6.). Lower panel shows the same dSTORM image after a mean filter was applied to reduce noise in the histogram of z-position to improve the reliability of the clathrin and actin height readout. We measured the overlap of clathrin and actin profiles by subtracting the upper position of actin from the lower position of clathrin. **(C)** x-z projected dSTORM image of a clathrin coat with its corresponding normalized pixel intensity histogram projected onto the x-axis unfiltered. Due to the image noise the measurement of clathrin coat width misses most of the image. The right

image shows the improved width measurement of the same clathrin coat after application of a median filter to smooth the histogram. **(D)** x-y projection dSTORM images corresponding to the x-z projections in Figure 2 A. The upper image corresponds to the first image in the row in Figure 2 A. Left images show clathrin (red), middle images actin (cyan) and the right image clathrin and actin merged, respectively. **(E)** x-y projection dSTORM images of clathrin (red) and N-WASP (rainbow) corresponding to the x-z projection in Figure 2 D and in Figure 2 E. **(A) – (E)** All scale bars are 100 nm.

Figure S2: Hypotonic media treatment of SK-MEL-2 cells endogenously expressing CLTA-TagRFP-T^{EN} and DNM2-eGFP^{EN}. (A), (C) and **(E)** Normalized cumulative distribution data for CLTA-TagRFP-T^{EN} and DNM2-eGFP^{EN} fluorescence lifetimes when associated with or not associated with each other. Lifetimes were recorded under isotonic media conditions and then recorded after 2 min or 10 min of media exchange. Plot legend provides respectively: mean lifetime ± SD, number of tracks, p-value determined in Kolmogorov-Smirnov test with significance compared to the control. **(B), (D)** and **(F)** show CME initiation rate, completion rate and percentage of persistent tracks plotted for sites in which DNM2-eGFP^{EN} and CLTA-TagRFP-T^{EN} were associated with each other. Tables below show the corresponding statistics. Mann-Whitney statistical test was used to compare CME initiation rates and completion rates. **(A)** and **(B)** Control conditions in which only isotonic media exchange was performed. n = 3-4 (cells) for each condition. Experiments were repeated 3 times. **(C)** and **(D)** Media were exchanged from isotonic to 225 mOsm hypotonic. For each of the following conditions: control, 2 min, or 10 min after media exchange, n = 6 (cells). **(E)** and **(F)** Media were exchanged from isotonic to 150 mOsm hypotonic. For each condition of the following conditions: control, 2 min

and 10 min after media exchange, n = 6 (cells). **(C) – (F)** Experiments were repeated 5 – 6 times. **(G)** Statistics for CME initiation rates, completion rates and percentage of persistent tracks for CLTA-TagRFP-T^{EN} associated with DNM2-eGFP^{EN} corresponding to Figure 3 G – I.

Figure S3: Effects of hypotonic media and concomitant CK666 treatment on CME progression. (A) Normalized fluorescence lifetime cumulative distribution data for CLTA-TagRFP-T^{EN} and associated DNM2-eGFP^{EN} for CK666 concentrations of 25 μM, 50 μM and 100 μM. Respective controls were 0.5% v/v, 1% v/v and 2% v/v DMSO. Fluorescence lifetimes were acquired after 2 minutes of treatment. Experiments were repeated 2-3 times. Kolmogorov-Smirnov statistical test was used. **(B)** Corresponding CME completion rates for CLTA-TagRFP-T^{EN} associated with DNM2-eGFP^{EN} in Figure 4 B and C. **(C)** Percentage of persistent tracks for CLTA-TagRFP-T^{EN} associated with DNM2-eGFP^{EN} for corresponding imaging data in Figure 4 B and C. **(D)** Corresponding CME initiation rates for CLTA-TagRFP-T^{EN} associated with DNM2-eGFP^{EN} in Figure 4 B and C. **(E)** Statistics for clathrin coat height and width for data in Figure 4 G when cells were treated with 2% v/v DMSO, 100 μM CK666 and 100 μM CK666 in 150 mOsm hypotonic media. **(F)** Plotted clathrin coat width in nm for data in Figure 4 G. **(G)** Ratio of clathrin coat height to width for data in Figure 4 G and Figure S3 F. **(B), (D)** and **(F)** Mann-Whitney statistical test was used. **(B) - (D)** and **(F)** bars show mean with SD.

Figure S4: Representative x-y projections of super-resolved clathrin coat associated with or without actin and/or a DNM2-eGFP^{EN} fluorescence signal. (A) – (D) x-y projection dSTORM images corresponding to the x-z projections in Figure 5 A, B, D and E. Left images show TIRF images of DNM2-eGFP^{EN}, middle images show super-resolved clathrin (red) in dSTROM and

right images show super-resolved actin (cyan), respectively. **(A)** Clathrin not associated with actin or DNM2-eGFP^{EN}. **(B)** Clathrin associated with DNM2-eGFP^{EN}, but lacking actin. **(C)** Clathrin associated with actin, but lacking DNM2-eGFP^{EN}. **(D)** Clathrin associated with actin and DNM2-eGFP^{EN}. **(A) – (D)** All scale bars are 100 nm. **(E)** Statistical significance of the difference in clathrin coat surface area between isotonic media and 75 mOsm hypotonic media. Mann-Whitney statistical test was used.

Figure S5: Effect of hypotonic media treatment on actin organization. (A) dSTORM image of CF-680 immunolabeled clathrin-coated structures (red) on the ventral cell surface when 75 mOsm hypotonic media was applied for 5 min. **(B)** Same area of the cell as in (A) showing the dSTORM image of phalloidin-AF647 labeled actin cytoskeleton (rainbow). **(C)** Same area of the cell as in (A) showing the corresponding DNM2-eGFP^{EN} conventional microscopy image. **(D)** Merged clathrin and actin dSTORM images from (A) and (B). Color bar shows actin position in the z-dimension. **(A) – (D)** All scale bars are 5 μm. **(E)** and **(F)** dSTORM x-y projection images corresponding to images in Figure 7 D and E. All scale bars are 100 nm. (**G)** Upper panel shows an example of asymmetrically organized actin around a clathrin-coated pit. Normalized pixel intensity histograms of clathrin (red) and actin (blue) from x-z and y-z projections. Measurement is the distance of the peak actin signal from the center of the clathrin coat. Actin is asymmetrically organized since the distance from the x-axis to the center is large compared to the distance to the y-axis. The lower panel shows an example of symmetrically organized actin around a clathrin-coated pit. Respective distances of the actin maximum to the center of the clathrin coat are much smaller. **(H)** Table with statistics for the data in Figure 7 I. Mann-Whitney statistical test compares asymmetry of actin under isotonic and hypotonic media conditions.

Supplementary movie 1: Movie of CLTA-TagRFP-T^{EN} (magenta) and DNM2-eGFP^{EN} (green) in SK-MEL-2 cells in isotonic media.

Supplementary movie 2: Movie of CLTA-TagRFP-T^{EN} (magenta) and DNM2-eGFP^{EN} (green) in SK-MEL-2 cells after 2 minutes of media exchange to 75 mOsm media.

Supplementary movie 3: Movie of CLTA-TagRFP-T^{EN} (magenta) and DNM2-eGFP^{EN} (green) in SK-MEL-2 cells after 10 minutes of media exchange to 75 mOsm media.

Supplementary movie 4: Movie of CLTA-TagRFP-T^{EN} (magenta) and DNM2-eGFP^{EN} (green) in SK-MEL-2 cells in isotonic media before treatment with CK666 and 150 mOsm hypotonic media.

Supplementary movie 5: Movie of CLTA-TagRFP-T^{EN} (magenta) and DNM2-eGFP^{EN} (green) in SK-MEL-2 cells in 150 mOsm hypotonic media with 100 μM CK666. Movie acquisition started 2 minutes after media exchange.

.

Figure S1

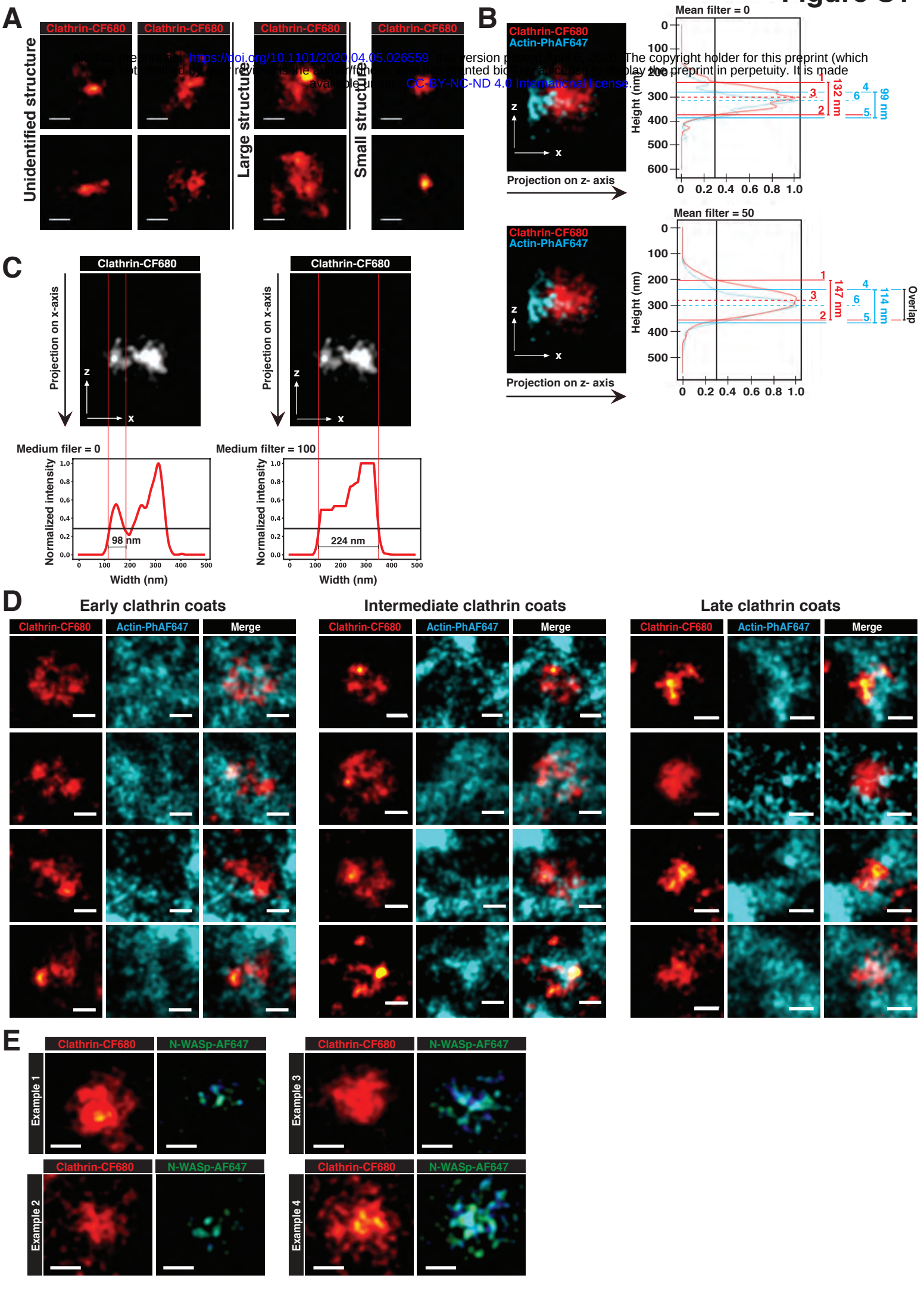

Figure S2

A

Isotonic media, 300 mOsm

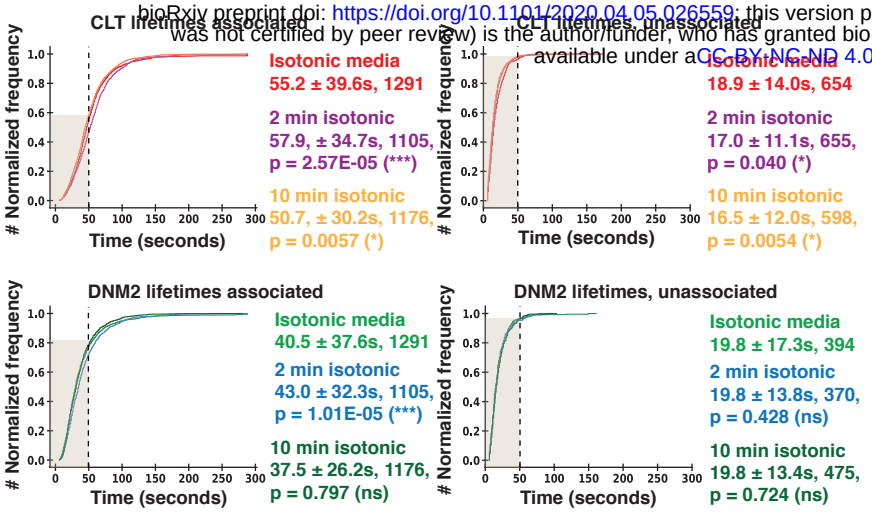

B

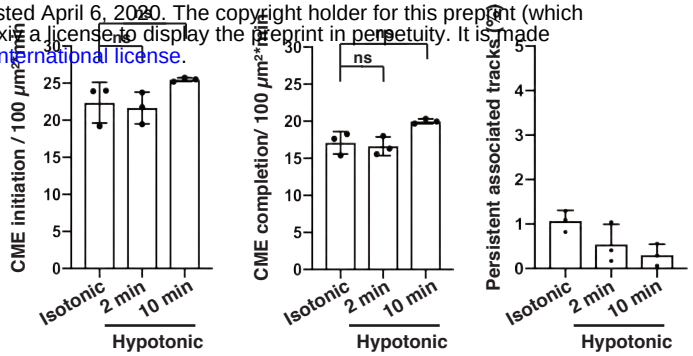

	Mean initiation rate ± SD (100 μm^2*min)	Mean completion rate ± SD (100 μm^2*min)	Mean persistent tracks (%) ± SD
Isotonic	19.19 ± 2.75	17.1 ± 1.51	1.1 ± 0.23
Isotonic, 2 min	19.46 ± 2.14	16.64 ± 1.26	0.54 ± 0.45
Isotonic, 10 min	25.22 ± 0.25	20 ± 0.33	0.30 ± 0.24

C

Hypotonic media, 225 mOsm

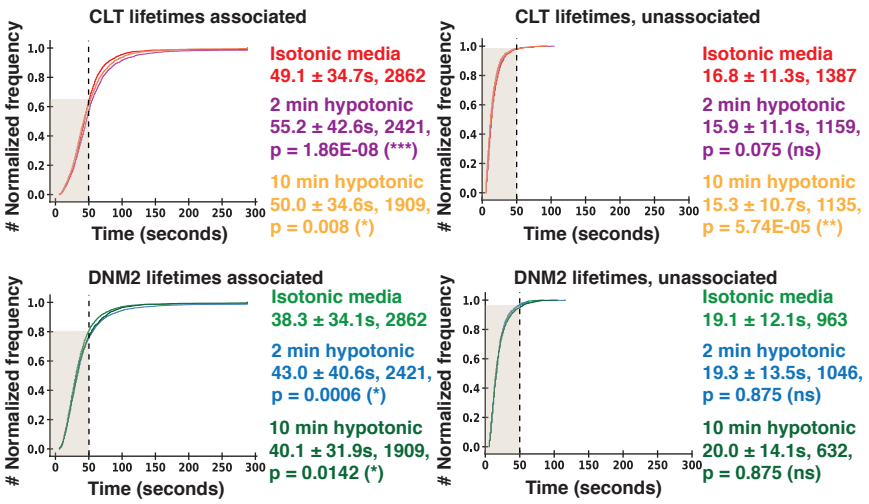

D

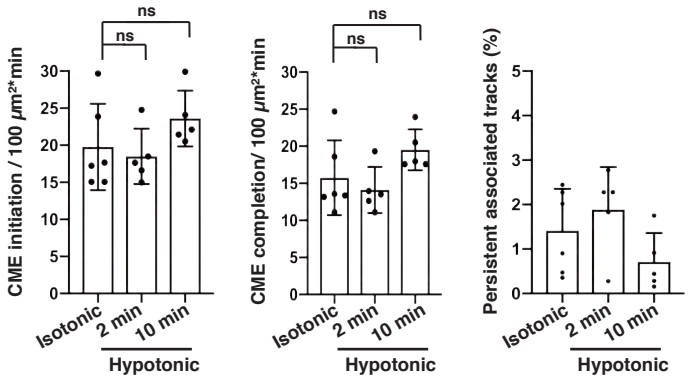

	Mean initiation rate ± SD (100 μm^2*min)	Mean completion rate ± SD (100 μm^2*min)	Mean persistent tracks (%) ± SD
Isotonic	19.76 ± 5.82	15.75 ± 5.03	1.41 ± 0.94
225 mOsm, 2 min	18.50 ± 3.73	14.10 ± 3.12	1.89 ± 0.96
225 mOsm, 10 min	23.61 ± 3.76	19.52 ± 2.76	0.71 ± 0.65

E

Hypotonic media, 150 mOsm

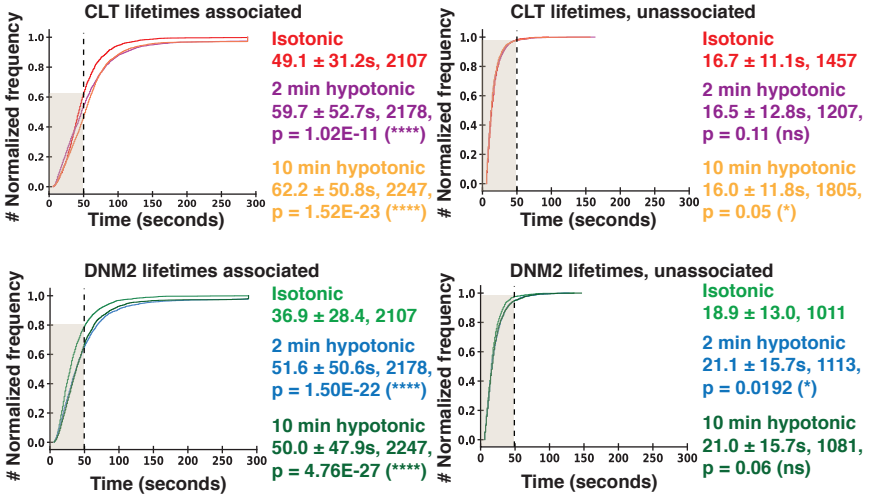

F

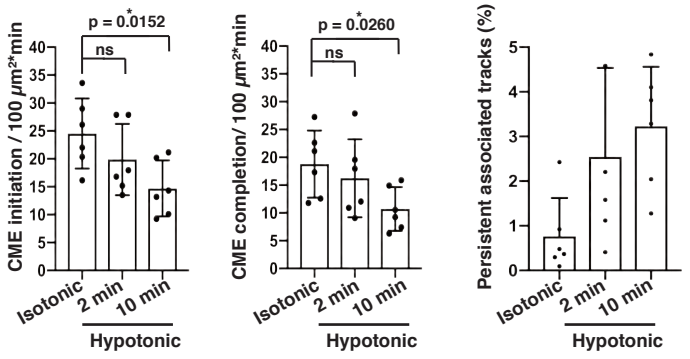

	Mean initiation rate ± SD (100 μm^2*min)	Mean completion rate ± SD (100 μm^2*min)	Mean persistent tracks (%) ± SD
Isotonic	24.53 ± 6.29	18.78 ± 6.03	0.77 ± 0.86
150 mOsm, 2 min	19.87 ± 6.39	16.24 ± 7.02	2.55 ± 1.99
150 mOsm, 10 min	14.70 ± 5.00	10.72 ± 3.92	3.23 ± 1.34

G

	Mean initiation rate ± SD (100 μm^2*min)	Mean completion rate ± SD (100 μm^2*min)	Mean persistent tracks (%) ± SD
Isotonic	22.18 ± 3.46	17.75 ± 3.43	0.65 ± 0.30
75 mOsm, 2 min	10.28 ± 1.48	5.32 ± 1.72	19.17 ± 9.21
75 mOsm, 10 min	9.54 ± 2.05	5.82 ± 2.07	11.45 ± 9.66

Figure S3

A

CK666 treatment; CLCA-TagRFP.T associated

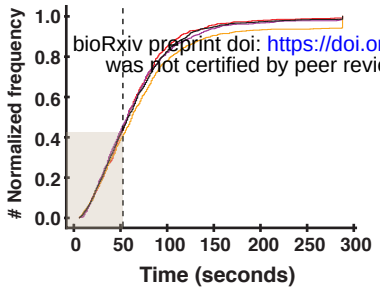

	Mean(s)	SD(s)	N. tracks	N. cells	p-value to pre CK666
pre CK666	68.0	48.8	1441	6	
CK666 25μM	66.2	45.4	744	6	0.7111
CK666 50μM	68.8	52.0	833	5	0.7925
CK666 100μM	78.9	66.2	835	8	0.0485

DMSO treatment; CLCA-TagRFP.T associated

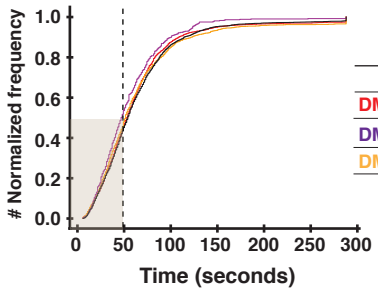

	Mean(s)	SD(s)	N. tracks	N. cells	p-value to pre DMSO
pre DMSO	65.2	50.0	2852	14	
DMSO 0.5% (v/v)	64.3	51.5	1469	5	0.2012
DMSO 1.0% (v/v)	66.3	56.7	1177	5	0.1405
DMSO 2.0% (v/v)	56.2	39.9	526	5	0.0011

CK666 treatment; DNM2-eGFP associated

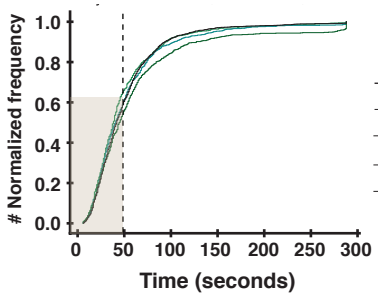

	Mean(s)	SD(s)	N. tracks	N. cells	p-value to pre CK666
pre CK666	52.6	42.3	1441	6	
CK666 25μM	51.1	44.6	744	6	0.0064
CK666 50μM	54.6	48.3	833	5	0.5346
CK666 100μM	64.7	64.1	835	8	0.0034

DMSO treatment; DNM2-eGFP associated

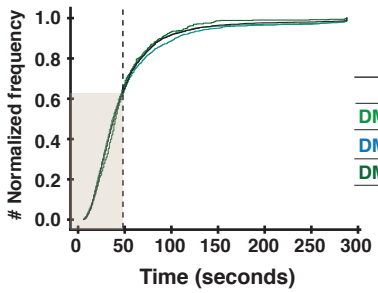

	Mean(s)	SD(s)	N. tracks	N. cells	p-value to pre DMSO
pre DMSO	51.0	45.9	2852	14	
DMSO 0.5% (v/v)	51.2	49.4	1469	5	0.5880
DMSO 1.0% (v/v)	54.4	52.6	1177	5	0.2858
DMSO 2.0% (v/v)	49.0	37.8	526	5	0.0583

B

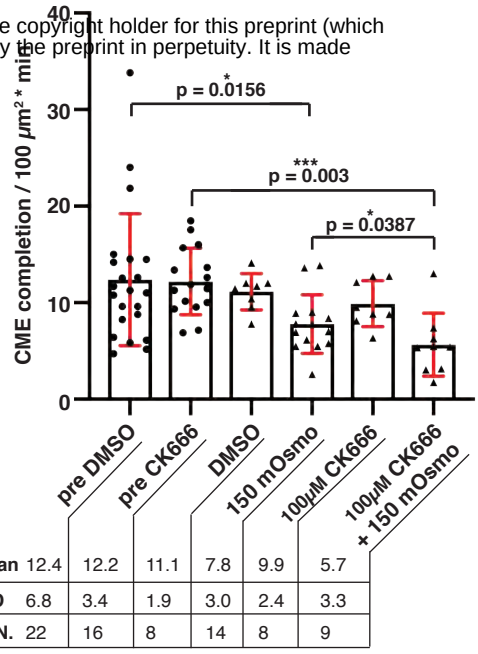

	pre DMSO	pre CK666	DMSO	150 mOsmo	100μM CK666	100μM CK666 + 150 mOsmo
Mean	12.4	12.2	11.1	7.8	9.9	5.7
SD	6.8	3.4	1.9	3.0	2.4	3.3
N.	22	16	8	14	8	9

C

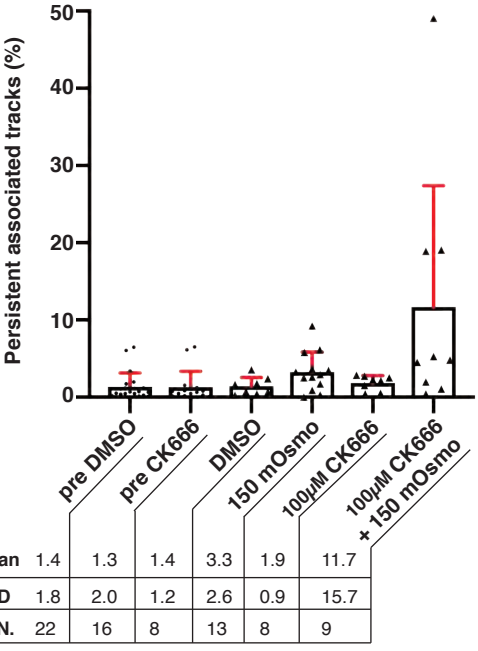

	pre DMSO	pre CK666	DMSO	150 mOsmo	100μM CK666	100μM CK666 + 150 mOsmo
Mean	1.4	1.3	1.4	3.3	1.9	11.7
SD	1.8	2.0	1.2	2.6	0.9	15.7
N.	22	16	8	13	8	9

D

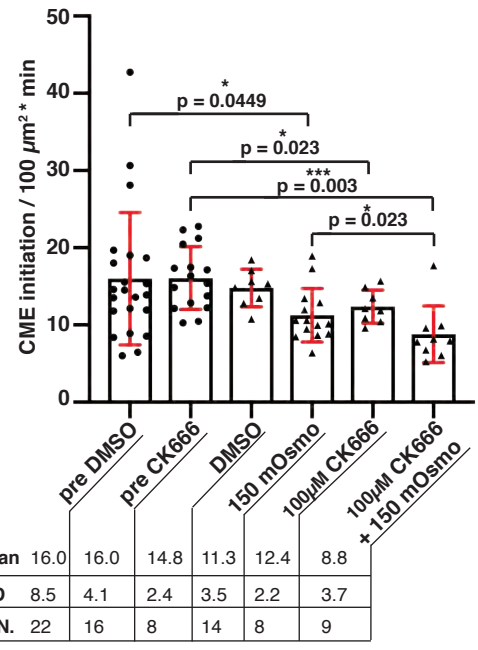

	pre DMSO	pre CK666	DMSO	150 mOsmo	100μM CK666	100μM CK666 + 150 mOsmo
Mean	16.0	16.0	14.8	11.3	12.4	8.8
SD	8.5	4.1	2.4	3.5	2.2	3.7
N.	22	16	8	14	8	9

E

	Mean height (nm)	SD (nm)	N. of values	Mean width (nm)	SD (nm)	N. of values
DMSO	98	21	154	177	30	154
100μM CK666	106	27	158	177	28	158
100μM CK666 + 150mOsmo	96	24	159	171	32	159

F

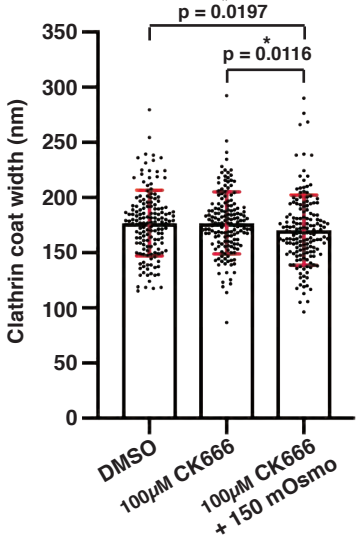

G

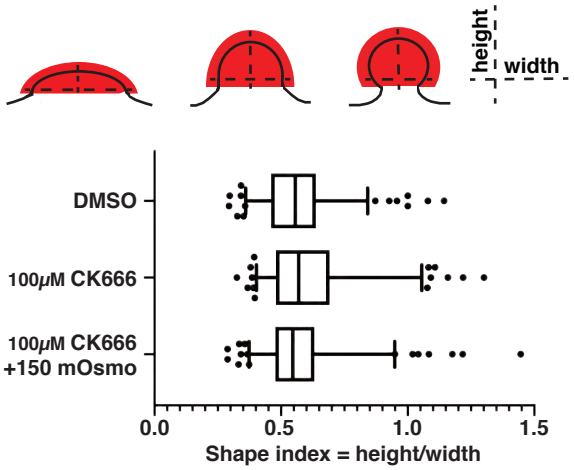

Figure S4

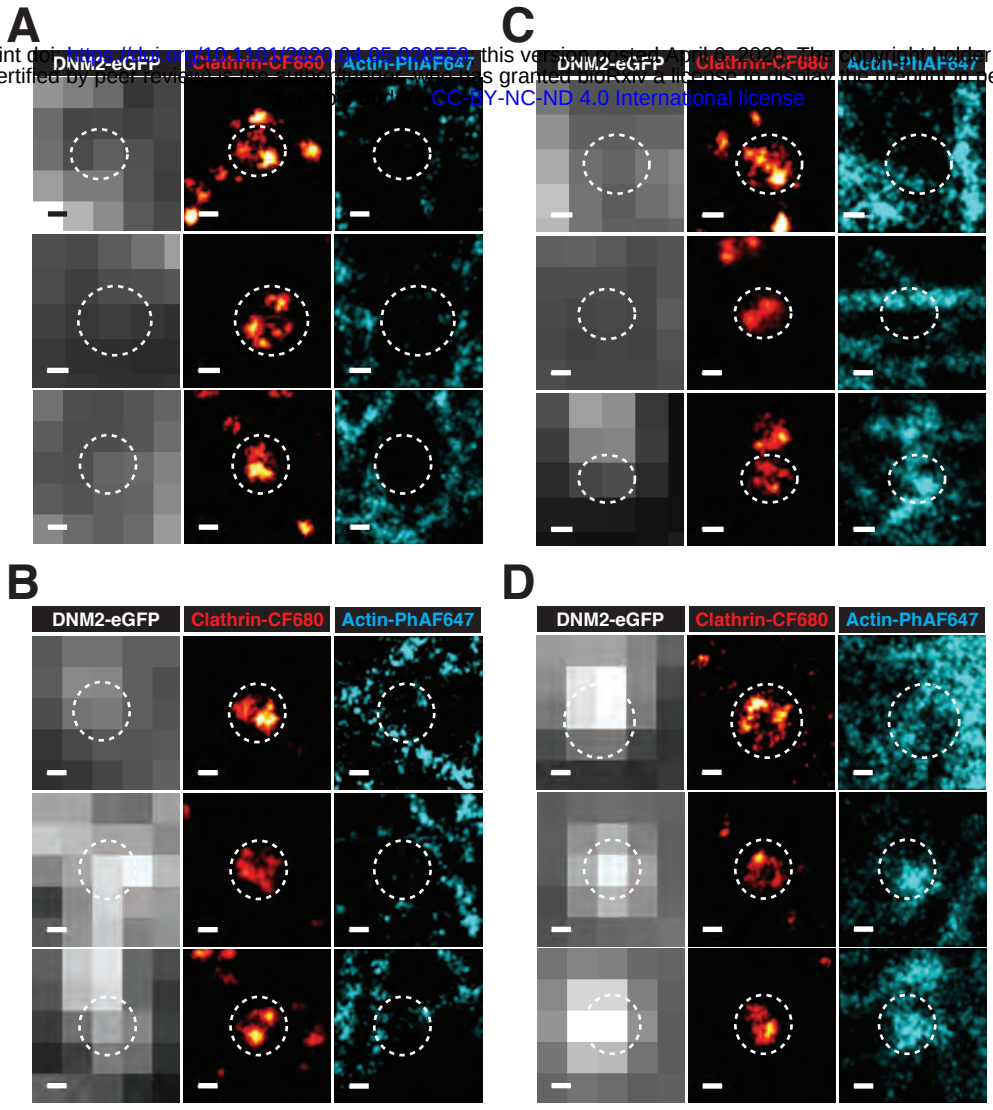

E

Surface area	Early	Intermediate	Fission	Late
W/o actin	0.0148 *	ns	ns	ns
With actin	0.0035 **	0.0027 **	< 0.0001 ****	ns

Figure S5

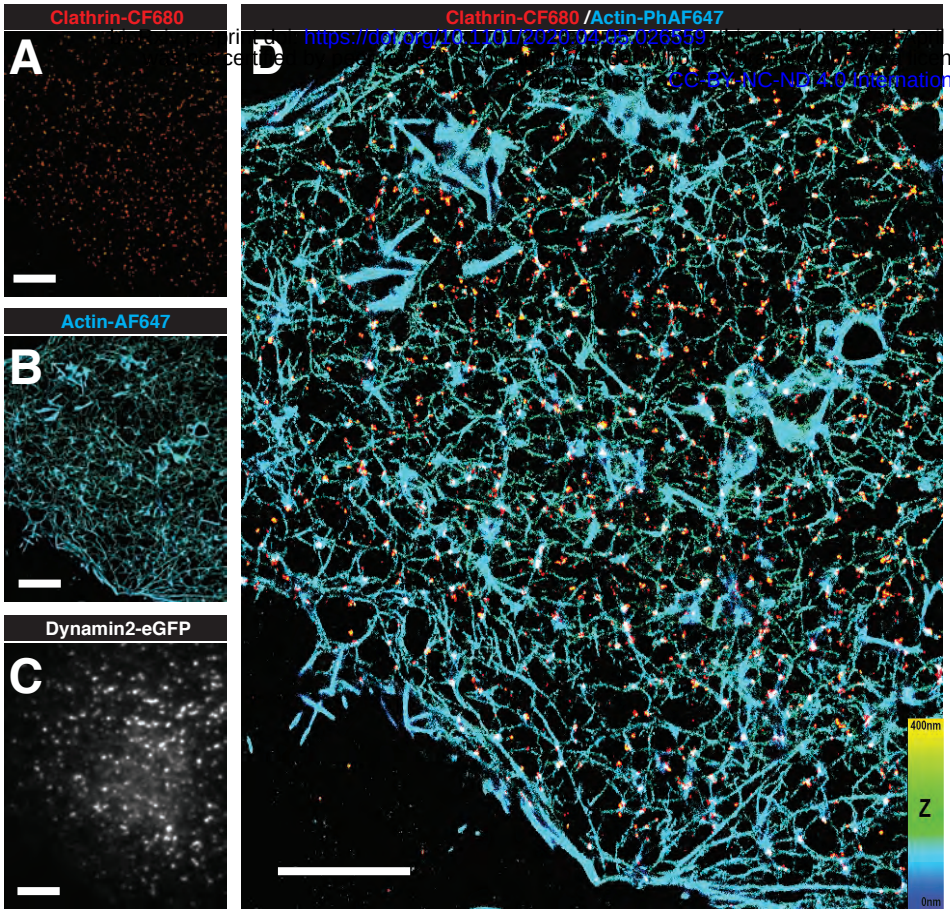

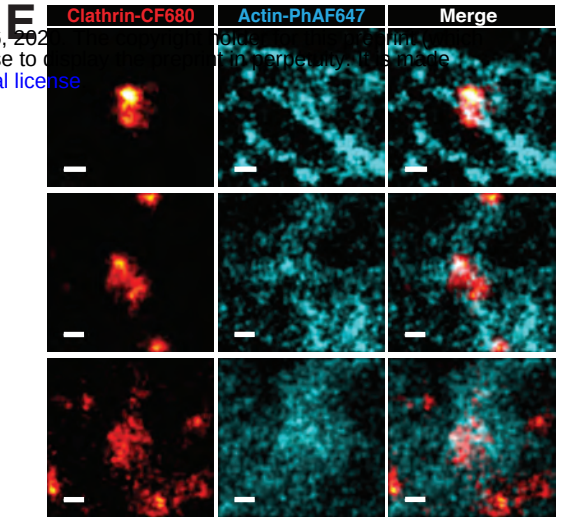

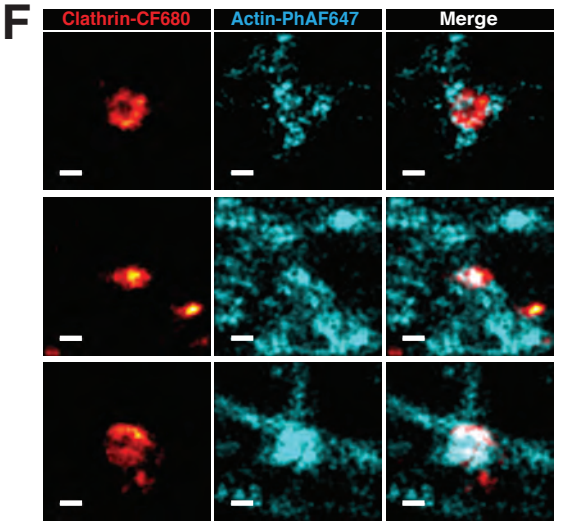

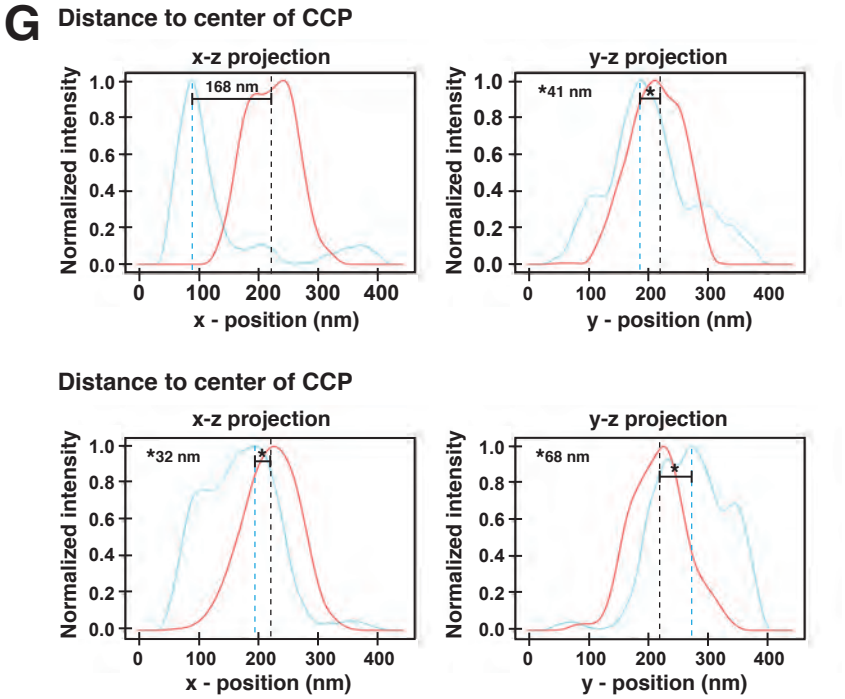

H

	75 mOsm			
	Mean deviation (nm)	SD (nm)	N. of values	p value
Early	72	44	155	< 0.0001
Intermediate	73	44	190	0.0087
Fission	70	45	236	ns
Late	72	45	401	0.0010

Table 1

		Isotonic media				Hypotonic media			
W/o Actin	Surface area	Early	IM	Fission	Late	Early	IM	Fission	Late
	Mean (nm^2)	62055	71048	68911	63762	69455	69606	80071	67607
	S.D. (nm^2)	16951	18854	23305	22419	20014	17353	26077	22633
	N.	85	31	23	117	85	70	72	132
With Actin	Surface area	Early	IM	Fission	Late	Early	IM	Fission	Late
	Mean (nm^2)	54811	61145	57936	58450	62666	68347	73414	59022
	S.D. (nm^2)	17328	17360	17268	22654	21515	21643	25636	22969
	N.	168	211	156	201	96	101	126	204
	p-value	** 0.0013	** 0.0028	* 0.0234	* 0.0263	* 0.0353	ns	ns	*** 0.0005

Table 2

	Isotonic			Hypotonic			Isotonic			Hypotonic		
	Height (nm)	**SD (nm)**	**N.**	**Height (nm)**	**SD (nm)**	**N.**	**Coverage (%)**	**SD (%)**	**N.**	**Coverage (%)**	**SD (%)**	**N.**
Early	123	29	167	158	48	96	66	25	163	76	21	88
Intermediate	131	34	211	146	42	101	68	23	209	76	20	100
Fission	135	30	156	161	39	127	64	22	153	69	20	126
Late	130	30	202	165	46	204	65	23	196	73	22	198